



# Comparison of schlieren-based techniques for measurements of a turbulent and wavy free surface

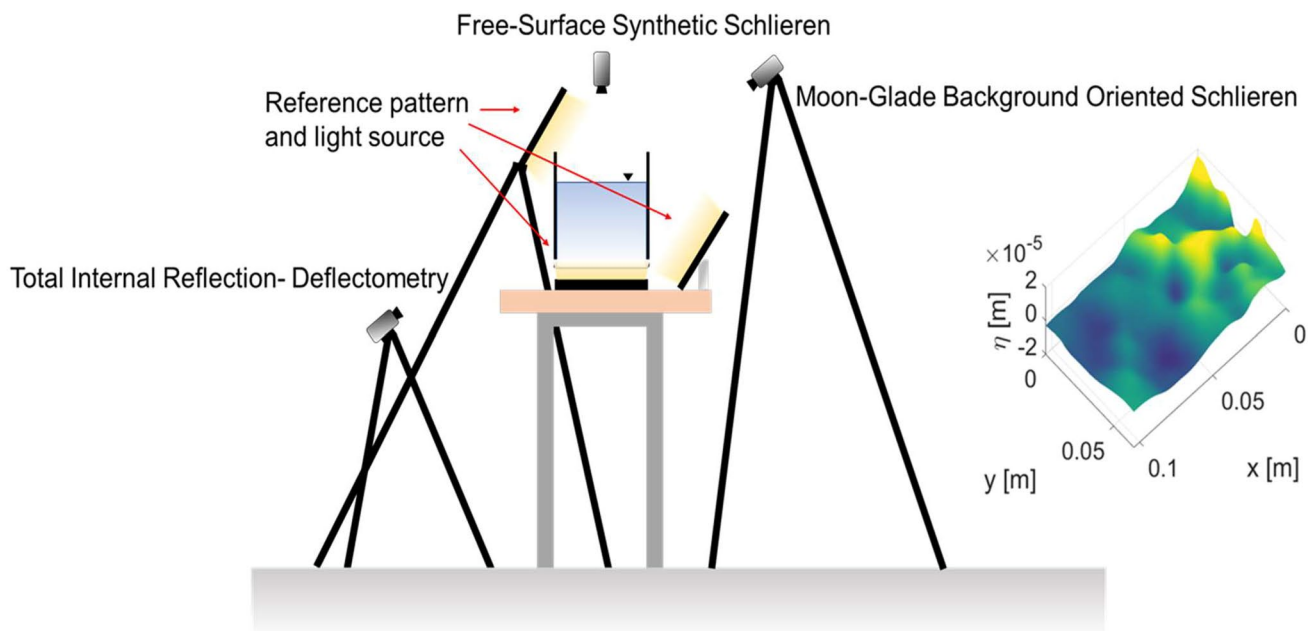
Vivek Bheeroo<sup>1</sup> · Tracy L. Mandel<sup>1</sup>

Received: 3 February 2023 / Revised: 13 April 2023 / Accepted: 6 May 2023 / Published online: 6 June 2023  
© The Author(s) 2023

## Abstract

The free surface at an air–water interface can provide information regarding bathymetric complexities, as well as the sub-surface flow. We present a comparison of the performance of two recent advances in light-based optical techniques for free surface measurements, total internal reflection-deflectometry and moon-glade background-oriented schlieren, with the more established method of free surface synthetic schlieren. We make use of an optical flow algorithm over the more traditional digital image correlation, in order to obtain higher spatial resolution data across the imaged free surface domain. The optical flow algorithm presents additional benefits, such as computational efficiency and robustness in capturing large displacements and straining of tracked features. The three optical techniques are assembled in synchronization to image two free surface conditions: (1) a free surface being impinged upon by an underlying turbulent, free-shear flow and (2) a random and irregular wave field induced by a free jet. Using the high-resolution measurements, we provide insight on the emergence of multiple free surface dynamics for a turbulent free surface. We present a comprehensive discussion on the benefits and drawbacks of each technique, including suggestions on the suitability of each technique for several experimental constraints.

## Graphical abstract



✉ Vivek Bheeroo  
vab1015@usnh.edu

<sup>1</sup> Center for Ocean Engineering, University of New Hampshire, Durham, NH 03824, USA

## 1 Introduction

The motivation to measure the deformations of a moving free surface has been reported extensively in the literature, at both small scales (coating/painting and food industries) and large scales (wind waves, ship wake and offshore engineering), as summarized by Gomit et al. (2013) and Moisy et al. (2009). Additionally, free surface phenomena are especially significant in nearshore areas, with their presence often linked to the occurrence of several turbulent processes (Dabiri and Gharib 2001). The characterization of the free surface can be undertaken through either intrusive or non-intrusive techniques. Regarding the former, instrumentation such as resistance type and pressure probes is often deployed in the field to monitor the temporal fluctuations of the free surface. The limitation of such techniques is that data can only be captured at discrete points within a domain, which are usually separated from one another by several centimeters at the least (Jain et al. 2021b). The importance of understanding surface dynamics has been a recent endeavor, as highlighted in review articles such as by Muraro et al. (2021). However, this is still a relatively unexplored field.

Non-intrusive techniques that have been used for the measurement of surface deformations have frequently revolved around optical methods that take advantage of light reflection or refraction (Cox and Munk 1954; Rosegen et al. 1998; Rupnik et al. 2015; Zhang 1996; Zhang et al. 1996; Zhang and Cox 1994). Some techniques have relied on the absorption properties of the liquid to measure its thickness (Mendez et al. 2017; Mouza et al. 2000), while others have used fluorescence-based methods (Collignon et al. 2022; Xue et al. 2019). Kurata et al. (1990) proposed an image-encoding approach, wherein scattered light emitted through a structured pattern is used to obtain a displacement field, through the comparison of the refracted images of the pattern obtained with flat and deformed surfaces. The displacement field is then used to compute the surface gradients, which in turn is integrated to obtain the surface profile. Moisy et al. (2009) furthered the work of Kurata et al. (1990) for the reconstruction of a deformed water surface by plane and circular waves. This method was labeled ‘free surface synthetic schlieren’ (FS-SS) and has since been used for various applications (Li et al. 2021; Mandel et al. 2017, 2019; Paquier et al. 2015; Pathommapas et al. 2019; Wildeman 2018). Shape from shading (SFS) has also been used for the reconstruction of water surfaces, wherein the gradual variation in shading is used to recover the shape of the features of interest (Chaudhari et al. 2014; Nie et al. 2021; Pickup et al. 2011).

Both the FS-SS and SFS methods present limitations. In the case of the FS-SS method, the technique will fail

in the presence of an obstructed region which makes the liquid surface optically inaccessible. For instance, the FS-SS method cannot be applied to laboratory experiments assessing flow over submerged obstacles. The SFS method is restricted to opaque liquid interfaces (such as the opaque appearance of the ocean surface due to its depth and the suspension of dirt and mud) as it has been shown that any shadow regions or highly specular patches led to inaccurate results (Pickup et al. 2011). Recent developments in reflection-based schlieren techniques can serve to possibly circumvent the foregoing issues. Vinnichenko et al. (2020) make use of the free surface as a mirror, in order to track the specular reflections of a reference pattern, and consequently reconstruct the moving surface. Their method is called moon-glade background oriented schlieren (M-G). Jain et al. (2021b, 2021c, 2021a) also visualize the movements of the water surface by using it as a specularly reflecting surface, but in a total internal-reflection sense, by imaging the underside of the free surface. This technique is called ‘total internal reflection-deflectometry’ (TIR-D). In both of these reflection-based techniques, any submerged artifact that does not occupy a significant portion of the water column does not affect the optical measurements. The hallmark of light-based optical techniques such as FS-SS, TIR-D and M-G is their simplistic setup. They only require a background reference pattern that are similar in style to those used in classic background oriented schlieren experiments, a light source, and a single camera. This contrasts with more involved setups that include LCD screens (phase measuring deflectometry; Zhang et al. 2021), projectors (fringe projection profilometry; Cobelli et al. 2009), specialized cameras (polarimetric slope sensing; Laxague et al. 2018), laser scanning beams (position sensing device-based techniques; Savelsberg and van de Water 2009) or seeding of the water body (stereocorrelation techniques; Turney et al. 2009).

Digital image correlation (DIC) techniques, specifically cross-correlation, have been used extensively for the tracking of features in FS-SS experiments. Other alternatives, such as Fourier demodulation (Diaz et al. 2022; Jain 2020; Jain et al. 2021b; Metzmacher et al. 2022; Shimazaki et al. 2022; Wildeman 2018), have also been performed on FS-SS experiments. However, the displacement fields produce unreliable data for steep surface gradients (Jain 2020). Recently, owing to advances in computer vision, optical flow (OF) algorithms have been applied for various flow problems. Notably, in the context of displacement field computation of background-oriented schlieren experiments, Atcheson et al. (2009) have shown that multi-resolution, multi-scale variants of gradient-based algorithms (Lucas and Kanade 1981; Horn and Schunck 1981) provide significantly better accuracy than DIC algorithms. The increased accuracy and spatial resolution of optical flow algorithms over cross-correlation was

also reported by Liu et al. (2015) for the case of experiments related to Oseen vortices and impinging air jets. Additional studies (Chetverikov et al. 2000; Ruhnau et al. 2005) have reported both the increased accuracy and efficiency of optical methods over cross-correlation techniques. Recently, Cakir et al. (2023) have compared the performance of OF algorithms over cross-correlation to measure supersonic flows using background-oriented schlieren. They found that the OF-based reconstructions revealed superior characteristics of resolution and sensitivity over cross-correlation. Their chosen algorithm is the Horn and Schunck (1981). Wu et al. (2019) applied the Farneback optical flow method (Farneback 2003) to compute surface velocity of water flow (SVWF) by subjecting a clear tank to adequate lighting and no shadows on the water surface. A regression analysis between the estimated SVWFs from the optical setup and the measured SVWFs using a propeller velocimeter showed good agreement, while producing a dense vector field.

The objective of the present study is to assess the performance of the recent advances in optical techniques (TIR-D and M-G) with a more established setup (FS-SS) for the reconstruction of a dynamic free surface. To the authors' knowledge, this is the first study to compare the performance of multiple optical techniques for surface reconstruction. The TIR-D and M-G techniques, due to their recency, are featured in limited studies other than the original work (Jain et al. 2022, 2021a, c; Kochkin et al. 2022; Mungalov and Derevyannikov 2021; Rudenko et al. 2022). These techniques have also gone unnoticed in reviews of optical techniques for surface measurements such as a recent comprehensive review by Gomit et al. (2022). The novelty of the present work is furthered by making use of a fairly atypical algorithm (Farneback algorithm) in the context of free surface reconstruction. To our knowledge, the comparison of the Farneback algorithm to cross-correlation has been performed just once (McIlvenny et al. 2022). We therefore compare the displacement field output between the Farneback algorithm and cross-correlation. The surface reconstruction procedure is performed for a rough and random surface. We induce the rough surface topography through a submerged jet angled toward the free surface, as well as by generating a random wavefield from an emergent jet overspill. This is in contrast with a majority of the previous water surface reconstruction exercises, where nearly-periodic and uniform waves/wave-like structures are observed (Chaudhari et al. 2014; Jain 2020; Jain et al. 2021b; Moisy et al. 2009; Wildeman 2018). Consequently, our analysis sheds new insight into (1) the hydrodynamics of a random wavefield that is induced by a collapsing vertical jet and (2) the turbulent manifestation of a submerged free-shear flow on a free surface and the resulting surface crispation.

The paper is organized as follows: we present an overview of the experimental setups and optical flow algorithm

in Sect. 2; the results and comparison of the optical techniques are featured in Sect. 3; we provide a discussion of the surface elevation behavior in Sect. 4; lastly, we formulate a conclusion based on our findings in Sect. 5. Detailed figures of the experimental setup are presented in "Appendix." We provide sample MATLAB code and animations of full experimental sequences of the free surface reconstruction for all experiments in the supplementary material.

## 2 Methods

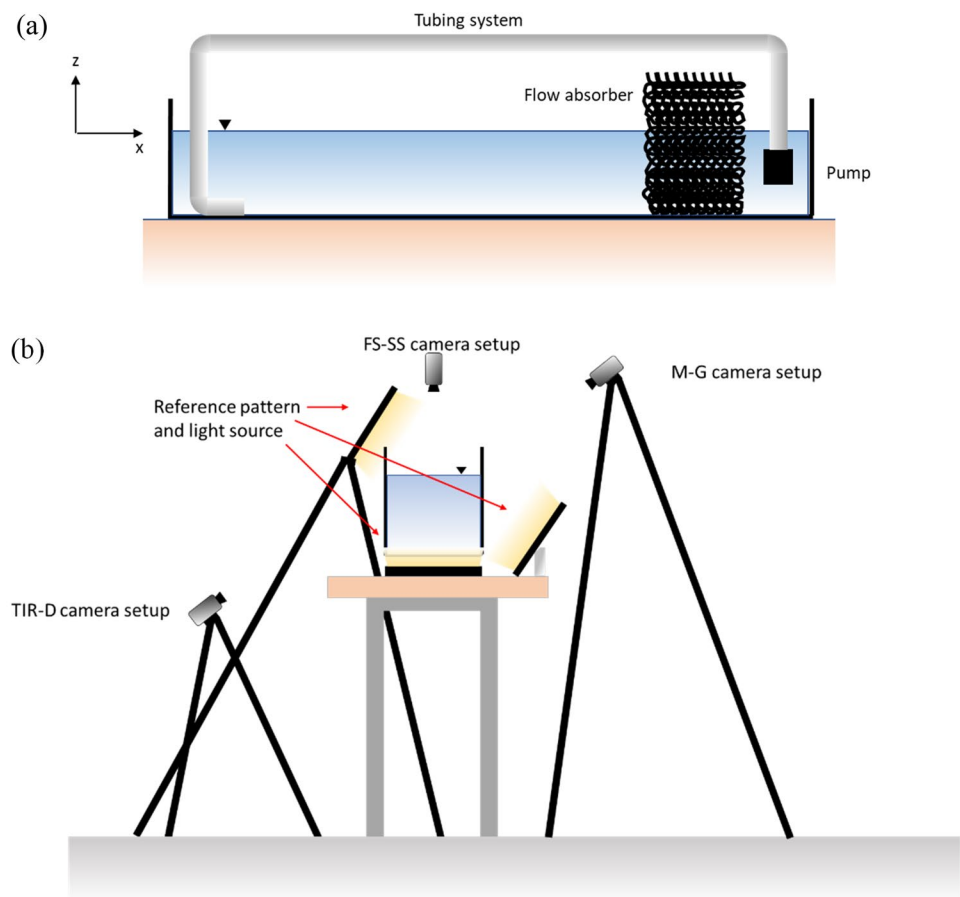
### 2.1 Experimental setup

Experiments are conducted in a 1.2 m long by 0.22 m wide by 0.3-m-deep acrylic tank. Recirculating flow is generated through a 1.27 cm ( $\frac{1}{2}$ " ) diameter tube that connects to a pump at the downstream end and discharges at the upstream end. A flow absorbing mesh is placed close to the pump to prevent any flow reflections as well as to dissipate vibration-induced flow motions from the pump. With this configuration, we ensure that flow is mostly uni-directional. A schematic of the tank is shown in Fig. 1a. A more detailed render of the experimental tank setup is shown in Fig. 21 in Appendix.

The pump discharge rate reaches a maximum of  $2.3 \times 10^{-4}$  m<sup>3</sup>/s, leading to a maximum pipe exit velocity of 1.8 m/s. The quiescent water depth,  $h_0$ , is kept constant at 0.175 m. The three optical techniques for the free surface reconstruction considered herein are free surface synthetic schlieren (FS-SS, Moisy et al. 2009), total internal reflection-deflectometry (TIR-D, Jain et al. 2021a, b, c), and moon-glade background-oriented schlieren (M-G, Vinichenko et al. 2020). The 3 techniques are used simultaneously to image a common free surface domain in the tank, as shown in Fig. 1b. Details of the physics underlying each measurement technique are presented in Sect. 2.2.

We use two FLIR Blackfly S USB3 (model number BFS-U3-28S5M-C) monochrome cameras for the M-G and TIR-D setups. Due to the close proximity of the TIR-D camera to the free surface, we use a fixed lens for TIR-D imaging (25 mm with aperture of  $f/1.4$ – $f/1.5$  and exposure time of 8000  $\mu$ s). A varifocal lens (12.5–75 mm with aperture of  $f/1.2$ – $f/16$  and exposure time of 10,000  $\mu$ s) is attached to the M-G camera to overcome the greater working distance from the camera to the free surface and provide magnification toward the  $0.22 \times 0.17$  m field of view. A FLIR Grasshopper USB3 (model number GS3-U3-32S4M-C) monochrome camera is used for the FS-SS setup with a similar lens to the M-G setup but operated at an exposure time of 6000  $\mu$ s. The three cameras are synchronized using SpinView FLIR FL3 and are triggered with a function generator (SIGLENT SDG 1032 X). This triple setup achieves a maximal acquisition

**Fig. 1** **a** Experimental setup. Pump is attached to the tubing system to generate a re-circulating flow. Flow absorber at downstream end prevents any reflection from the end-wall and dissipates any vibration-induced flow motions due to the pump. **b** Triple camera setup directed at the water surface to track surface motions. Each camera setup tracks the distortions of a reference pattern that is illuminated by LED panels



rate of 50 frames per second. The experiments are conducted for just over a minute, leading to 3072 frames per experimental run.

A monochromatic checkerboard design is used as a background reference pattern for each technique, with a grid size of 2.5 mm. This grid size is chosen because the resulting checkerboard pattern captures adequate spatial resolution without collecting significant ambient noise from water residuals/debris. The background pattern is fixed to an LED panel (RALENO LED) to provide illumination, with the following operating conditions: 100% brightness, 5600 K Color Temperature. Surrounding background illumination is suppressed by extinguishing all ceiling lights in the laboratory to ensure no caustic effects at the air–water interface, as well as to avoid interference with the LED panel brightness. Due to the multiple LED panels being used in the triple setup (see Fig. 1b), the light source from the FS-SS setup would interfere with the specular reflection properties of the M-G setup. To prevent this optical interference, we attach 2 types of bandpass filters to 2 of the imaging setups: a bandpass filter with narrow wavelength transmission around the central wavelength (CWL) of 525 nm for the M-G camera, and a bandpass filter with a CWL of 633 nm for the FS-SS setup. A gel filter of similar wavelength to the relevant

imaging setup is equipped onto the LED panel. In this way, the imaging system acquires transmitted wavelength that is constrained to the CWL. Due to the lack of optical interference between the TIR-D and other setups, the TIR-D imaging system does not require bandpass filters.

The free surface is perturbed by the recirculating flow in two ways: (1) turbulent free-shear flow emanating from a submerged jet that impinges the underside of the free surface; and (2) an overspill, emergent jet that induces gravity-capillary like wave forms that propagate radially along the length of the tank. A schematic of both flow conditions is shown in Fig. 2. The flow speed of both flow conditions is modified by varying the pump discharge rate. The Reynolds number is then computed as

$$\text{Re} = \frac{UD}{\nu}, \quad (1)$$

where  $U$  is the exit velocity of the pipe,  $D$  is the pipe diameter and  $\nu$  is the kinematic viscosity of water ( $10^{-6} \text{ m}^2/\text{s}$ ). Table 1 summarizes the experiments for both flow conditions.

The flow for each flow condition is characterized as either ‘slow,’ ‘medium’ or ‘fast’ based on the corresponding Reynolds number. Due to the nature of the free jet in the overspill

**Fig. 2** Surface perturbation techniques. **a** Submerged jet angled at approximately 45° above the horizontal, **b** Overspill flow-induced gravity capillary waves. The surface elevation,  $\eta$ , is the departure of the water surface from the quiescent state

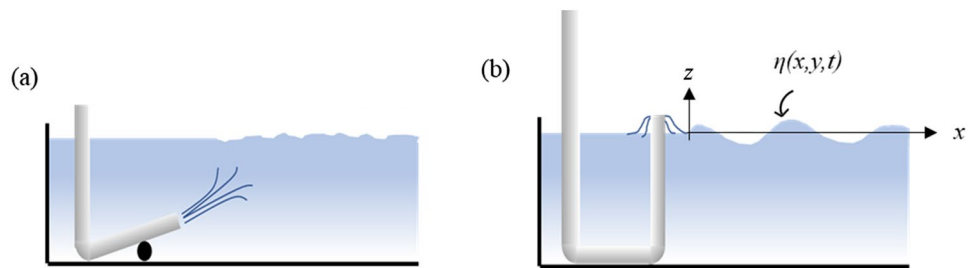


**Table 1** Experimental matrix with experiment naming convention

Experiment index	Flow condition	Reynolds number	Flow type
J1	Submerged jet	3800	Slow
J2	Submerged jet	6400	Medium
J3	Submerged jet	8600	Fast
W1	Overspill flow	3800	Slow
W2	Overspill flow	6400	Medium
W3	Overspill flow	8600	Fast

flow cases, the  $Re$  is not particularly physically meaningful for these cases. However, the parameter establishes a contrasting surface behavior within the overspill flow cases. Depictions of a detailed model of the tube network setup for both surface topographies shown in Fig. 2 are illustrated in Fig. 22 of Appendix.

## 2.2 Measurement techniques

The premise of the 3 measurement techniques (FS-SS, TIR-D, M-G) is as follows: the apparent distortions observed in a reference pattern due to a moving free surface are digitally compared to a still reference background for an undisturbed free surface. This leads to the displacement field,  $\tilde{u}$ , of the surface features. The displacement field is then related to the surface gradients linearly, as is shown in Sects. 2.2.1–2.2.3. Finally, the surface gradients are integrated in a least-squared sense to obtain  $\eta$ . This is performed with a MATLAB implementation of an inverse gradient operation (Wildeman 2018).

TIR-D and M-G use the free surface as a mirror: the distortions to the reflected reference pattern are tracked from the moving free surface in a specular way. In the case of M-G, the specular reflections occur at the free surface exposed to the atmosphere, while TIR-D takes advantage of the underside of the free surface in a total internal reflection configuration. FS-SS uses the free surface as a lens, in order to track the distortions to the reference pattern through light refraction across the air–water interface.

### 2.2.1 FS-SS setup

The FS-SS setup is shown in Fig. 3. The camera is placed directly above the domain of interest along the free surface with a field of view of  $0.22 \times 0.17$  m. The reference pattern is placed below the tank, at a distance of  $h_a$  to the tank bottom. The distance from the water surface to the reference pattern is  $h_p$  while the camera is set at a distance  $H_{cam}$  from the reference pattern.

We set  $h_a$  at 0.015 m.  $h_p$  is computed from (2).

$$h_p = h_o + \frac{n'}{n_{ac}} h_{ac} + \frac{n'}{n'} h_a \tag{2}$$

where  $n'$  and  $n_{ac}$  are the refractive indices of air and acrylic, respectively, and  $h_{ac}$  is the tank bottom thickness. From (2),  $h_p$  is 0.22 m and  $H_{cam}$  is set at 1.56 m. From Moisy et al. (2009), the displacement field from the refracted image of the distorted reference pattern is connected to the surface gradients in the  $x$  and  $y$  direction through (3).

$$\nabla \eta = -\tilde{u} \left( \frac{1}{\alpha h_p} - \frac{1}{H_{cam}} \right) \tag{3}$$

where  $\alpha$  is related to the refractive indices of air and water and taken to be 0.25,  $\eta$  is the departure of the free surface from the quiescent state and  $\tilde{u}$  is the displacement field. An important assumption regarding the FS-SS setup is for  $H_{cam}$  to be much larger than the field size,  $L$ . The ratio of these two parameters yields a maximum paraxial angle,  $\beta_{max}$ . This is verified for our setup, as shown by (4).

$$\beta_{max} = \frac{L}{\sqrt{2} H_{cam}} = \frac{0.22}{\sqrt{2} * 1.56} = 0.0997 \tag{4}$$

From (4), the paraxial angle matches the criterion outlined by Moisy et al. (2009), wherein  $\beta_{max} \ll 1$ .

### 2.2.2 TIR-D setup

The TIR-D setup is shown in Fig. 4. The camera and reference pattern are placed on opposite sides of the tank, below



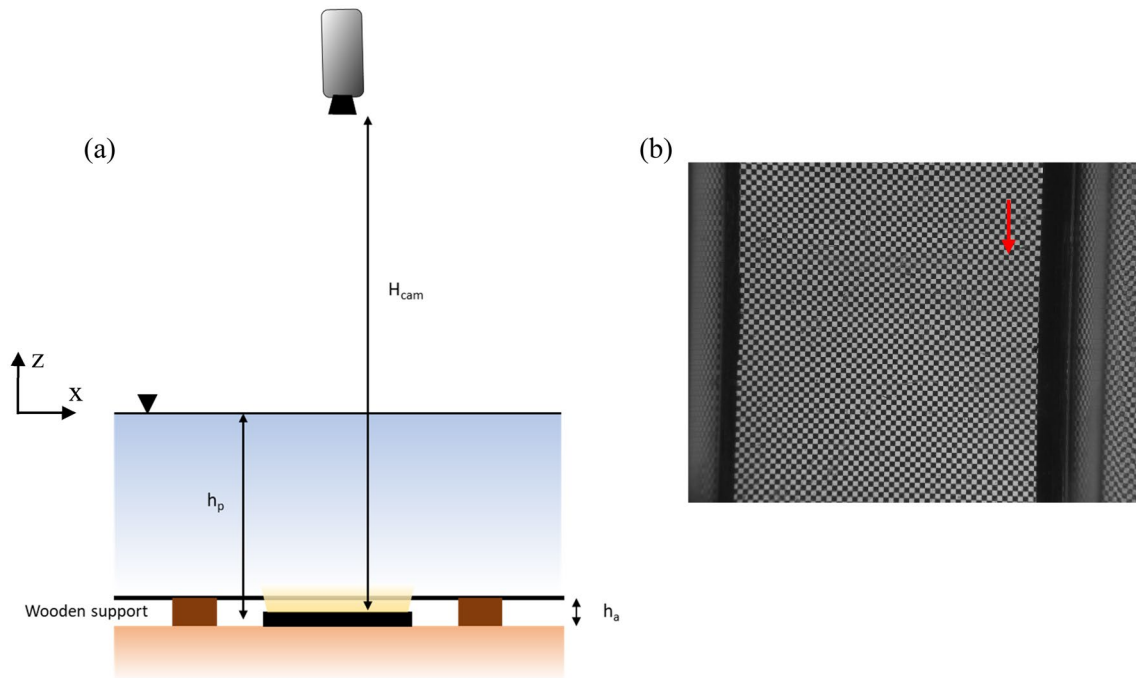


**Fig. 3** **a** Setup for FS-SS method. The camera is placed at a distance  $H_{cam}$  above the reference pattern. The reference pattern is placed below the tank, at a distance  $h_p$  from the water surface. The tank bottom is elevated from a horizontal surface with the use of wooden sup-

ports, in order to create a gap,  $h_a$ . The water surface acts as a lens to capture the distortions to the reference pattern. **b** Raw image from FS-SS setup. Direction of flow motion indicated with red arrow

the water line, and are directed at the underside of the moving free surface at an incident angle,  $\theta$ . We measure the incident angle as follows:

$$\theta = \tan^{-1} \left( \frac{x_i}{y_i} \right) \tag{5}$$

where  $x_i$  and  $y_i$  are the horizontal and vertical distance between the camera and the centerline of the water surface (in the  $y$ - $z$  plane). From Jain et al. (2021a, b, c), for specular reflection in a total internal reflection configuration to occur, (5) needs to be greater than a critical angle  $\theta_c \approx 48.75^\circ$ . From our experiments, we achieve an incident angle of around  $60^\circ$ .

The displacement field from this configuration is related to the surface gradients in  $x$  and  $y$  by (6).

$$\nabla \left( e^{\frac{yT}{h_o}} \eta \right) = -\frac{e^{\frac{yT}{h_o}}}{2h_o} \tilde{u} \tag{6}$$

where  $T=0.5\sin 2\theta$  and  $\tilde{u}$  is the displacement field. It is noted that the integrated results from (6) need to be divided by the factor  $e^{\frac{yT}{h_o}}$  to obtain the final height,  $\eta$ .

### 2.2.3 M-G setup

The M-G setup is shown in Fig. 5. The camera and background pattern are placed above the water line, pointed toward the free surface. A distance  $L=0.5$  m separates the background pattern from the centerline (along the  $x$  direction) of the domain of interest. We measure the camera's elevation angle with respect to the tank centerline to be about  $33^\circ$ , while the light source has an elevation angle of  $41^\circ$ . This camera angle is chosen as an intermediate tradeoff between image resolution and blurring effect.

The displacement field  $\tilde{u}$  is related to the surface gradients by (7).

$$\tilde{u} = 2L\nabla\eta \tag{7}$$

Vinnichenko et al. (2020) suggest two ways of computing  $\eta$ . (7) can be re-arranged in order to integrate  $\nabla\eta$  in a least-square sense. Alternatively, the gradients of  $\tilde{u}$  is applied to the Poisson equation, which is then solved for  $\eta$ . This is shown in (8).

$$\frac{\partial^2 \eta}{\partial x^2} + \frac{\partial^2 \eta}{\partial y^2} = \frac{a_{back}}{2La_{surf}} \left( \frac{\partial \tilde{u}_x}{\partial x} + \frac{\partial \tilde{u}_y}{\partial y} \right) \tag{8}$$

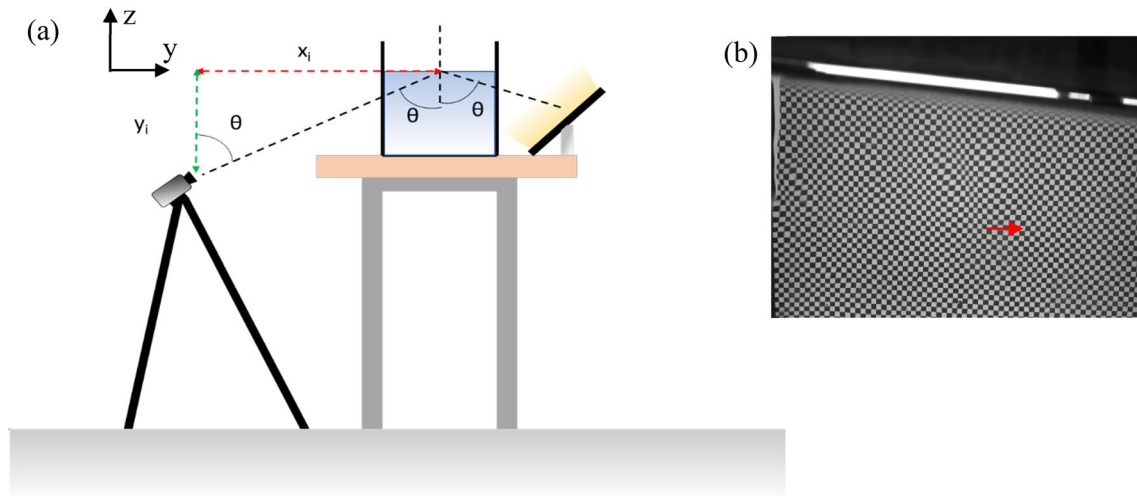
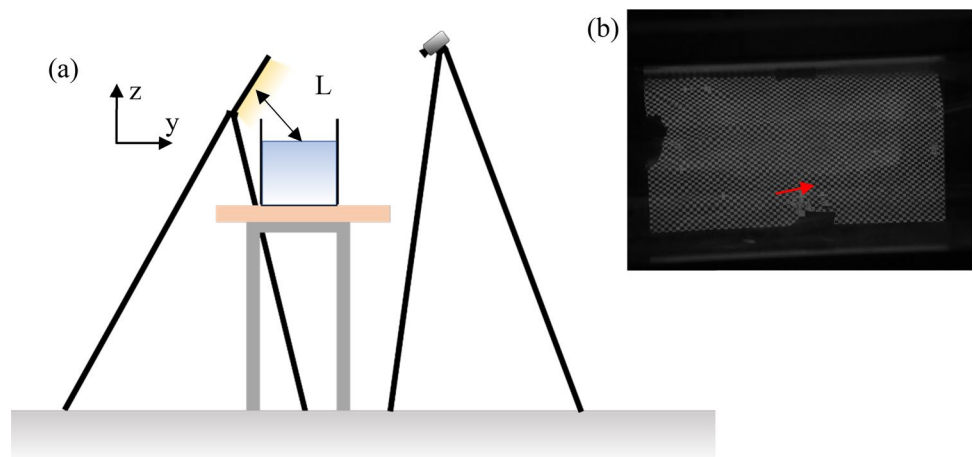


**Fig. 4** **a** Setup for TIR-D method. The underside of the water surface is used as a mirror to track distortions to the reference pattern. The incident angle is the inverse tangent of the ratio of the horizontal distance between the camera and the mid-way point of the water surface,

$x_i$  to the vertical distance between the camera and the water surface,  $y_i$ , and the **b** raw image from TIR-D setup. Direction of flow motion indicated with red arrow

**Fig. 5** **a** Setup for M-G method. The water surface is used as a mirror to track distortions to the reference pattern. The camera and background pattern sit above the waterline. The distance separating the background pattern and the water line is  $L$ . **b** Raw image from M-G setup. Direction of flow motion indicated with red arrow



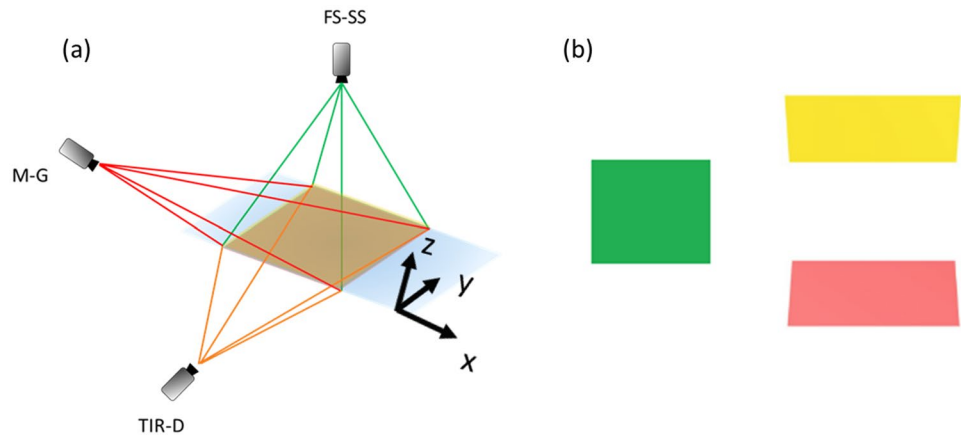
where  $a_{back}$  and  $a_{surf}$  are the image resolution in the background pattern plane and the liquid surface plane, respectively. The M-G setup is seen to be sensitive to illumination intensity: the presence of background illumination significantly affects the specular reflection properties of the free surface. As a result, the tank bottom (and any submerged features) appears within the M-G imaging output, due to the refraction of light across the air–water interface. This acts as a shadow region within the optical acquisition, rendering the displacement field computation inaccurate. It is therefore important to maintain no background illumination and to operate the LED panel at the brightest intensity. Additionally, adequate focal depth is required from the M-G camera to minimize patches of image blur.

### 2.2.4 Triple setup

The 3 surface measurement techniques (FS-SS, TIR-D, M-G) are used in conjunction to capture the free surface perturbations. We define the coordinate system such that  $x$  is along the streamwise direction of flow,  $y$  is along the transverse direction and  $z$  is perpendicular to the free surface pointing upwards (Fig. 6a).

The cameras are directed to approximately the same area of the free surface domain and are calibrated to capture identical perimeters on the free surface. A detailed model of the triple setup is shown in Fig. 23 of Appendix. The calibration process also allows for the perspective correction of the TIR-D and M-G frames in a projective transform fashion. The calibration is performed by imaging a checkerboard

**Fig. 6** **a** Triple setup for measuring free surface perturbations with coordinate axis shown. Cameras are angled to face the same domain. Spatial coordinates are shown. **b** Domain perspective output from the 3 measurement setups. Perspective corrections are required for the TIR-D and M-G domains. Colors are consistent with **a**



pattern (printed onto 0.1 mm thick transparency) that is rested onto a still free surface. Due to the geometrical setup of the FS-SS camera, no perspective correction needs to be performed on the FS-SS frames. The field of view essentially lies in the  $x$ - $y$  plane. The perspective projections for the TIR-D and M-G setup, as well as the orthonormal projection from the FS-SS setup are shown in Fig. 6b.

Two passes of image rectification are performed on the TIR-D and M-G image acquisitions. First, a geometric projective transformation is applied to correct for the image perspective (see Fig. 6b). Second, an intensity-based image registration approach is applied to the projective-transformed TIR-D and M-G images with respect to the FS-SS image acquisition. The two image registration passes allow for the TIR-D and M-G images to be interpolated to match the domain size and orthonormal projection of the FS-SS output. This allows for the direct comparison of  $\eta$  values between each technique. The spatial resolution of the data collection domain is of 10.4 cm in the streamwise direction and 6.5 cm in the transverse direction. This spatial extent is determined sufficient to capture the length scales of the various surface features. A schematic of the domain of data capture relative to the flow input is shown in “Appendix.”

## 2.3 Displacement field computation

### 2.3.1 Optical flow and the Farneback algorithm

The referenced studies involving free surface reconstruction (Jain et al. 2021b; Moisy et al. 2009; Vinnichenko et al. 2020) compute the displacement field using cross-correlation algorithms. Herein we consider optical flow (OF) as an alternative. OF is a method of feature tracking that does not rely on the injection of tracers in the fluid of interest. The algorithm relies on two hypotheses: (1) based on the gray level constancy assumption, the gray level is conserved in its displacement (Brox et al. 2004), i.e. in a

Lagrangian sense, and (2) adjacent points within the image move in a similar way.

For a 2D ( $x$ - $y$ ) plane, a pixel at location  $(x, y, t)$  with intensity  $I$  will move by  $\Delta x$  and  $\Delta y$  over a time interval  $\Delta t$  (corresponding to the time interval between two frames for instance). The brightness constancy constraint is then given by (9).

$$I(x, y, t) = I(x + \Delta x, y + \Delta y, t + \Delta t) \quad (9)$$

It is noted that (9) is a mathematical expression of hypothesis 1. By applying a Taylor series expansion to (9) and truncating the higher order terms, the following constraint equation is obtained:

$$\frac{\partial I}{\partial x}u + \frac{\partial I}{\partial y}v + \frac{\partial I}{\partial t} = 0 \quad (10)$$

where  $u$  and  $v$  are the optical flow vectors along the  $x$  and  $y$  directions. (10) is the fundamental equation of optical flow and is often referred to as the optical flow constraint equation. The Farneback method (Farneback 2003) is an algorithm designed to solve (10). The major difference between the Farneback algorithm and other classic optical flow algorithms such as Horn-Schunk and Lucas-Kanade is that the Farneback algorithm expresses the gray level in an image as a binary quadratic polynomial. Further, the Farneback algorithm is a dense optical flow (DOF) algorithm, as opposed to Horn-Schunk and Lucas-Kanade, which are Sparse Optical Flow algorithms. These differences ensure that the output from the Farneback algorithm is of greater accuracy than other optical flow methods (Farneback 2003; Wu et al. 2019). For brevity, we direct the reader to Wu et al. (2019) for the complete derivation of (10) as well as a detailed overview of the Farneback algorithm. Additionally, from here on, we refer to DOF as simply OF. We also use the terms digital image correlation, cross-correlation and PIV interchangeably.



We utilize a MATLAB (The MathWorks Inc. (2022)) implementation of the Farneback algorithm (Farneback 2003). The input image is decomposed into multiple layers, where each layer has a lower resolution compared to the previous layer. A greater number of layer decomposition allows for the algorithm to track larger displacements. The 5 main adjustable properties of the algorithm are as follows:

1. Number of pyramid layers: Number of layer decomposition to the original image.
2. Image scale: This parameter specifies the rate of down-sampling at each pyramid layer.
3. Number of search iterations: The algorithm performs an iterative search for key points at each layer until convergence is achieved.
4. Size of pixel neighborhood: Choice of neighborhood size determines the blurred motion. Blur motions yields a more robust estimation of optical flow, since a motion blurred image retains information about motion that parameterizes the blur (Dai & Wu 2008).
5. Averaging filter size: A Gaussian filter of size (Filter size<sup>2</sup>).

We use the default values for the number of pyramid layers, image scale and number of search iterations (3, 0.5, 3, respectively). The size of pixel neighborhood is chosen as 10 (twice the default value), to account for high displacements, and the filter size is taken as 45 pixels to ensure that a smooth displacement field is obtained for the surface reconstruction process given by either (3), (6) or (8). A sensitivity analysis from our experiments indicates a lack of variation in the displacement field output for the first 3 parameters, while the filter size affects the level of smoothness on the

displacement field. The displacement field output does not change significantly for pixel neighborhood sizes less than 25, as shown in Sec. 2.3.2.

### 2.3.2 Performance of the Farneback algorithm versus cross-correlation algorithm

As outlined earlier, there is a lack of robust comparison performed from the literature between DIC and Farneback algorithms. This is shown in this section for the context of displacements fields of a free surface. PIVlab (Thielicke and Sonntag 2021) is used to perform cross-correlations, due to its popularity and for consistency of programming language background (MATLAB) with the present implementation of the Farneback algorithm. Each cross-correlation exercise is computed with 2 passes, each using an FFT window deformation. A standard deviation filter and local median filter are applied to the PIV displacement vector output. The major advantage posed by the Farneback algorithm over cross-correlation is the denser spatial resolution from the former. This is shown in Fig. 7, for the displacement field computed for one of the wave experiments collected using the TIR-D setup. It is noted that only every 12th data point in the *x* and *y* direction are shown for the OF output, in order to be able to visualize individual vectors.

It is seen from Fig. 7 that the density of the displacement field output from cross-correlation is sensitive to the choice of interrogation window size. The smallest interrogation windows from the cross-correlation algorithm result in the highest displacement vector density amongst the cross-correlation results. This is at the expense of a loss of higher displacement data, as shown by a displacement magnitude plot in Fig. 8. Hence there is a clear trade-off between displacement vector density and computation/retention of higher

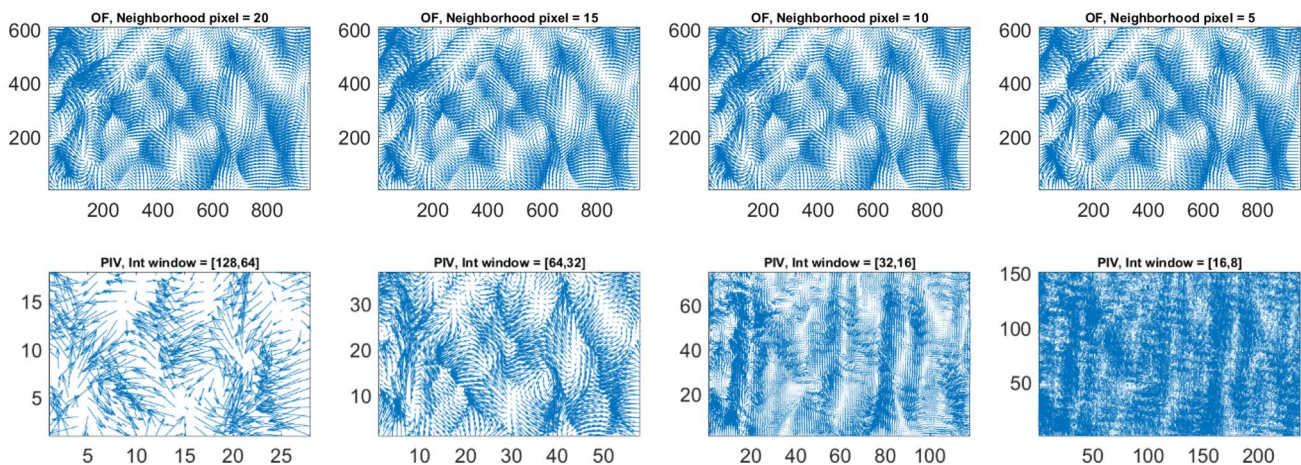


**Fig. 7** Comparison of displacement vector density between Farneback algorithm and PIV algorithm with varying interrogation window sizes. Every 12th element is shown in the OF figures due to

high arrow density. 2 passes are applied for each cross-correlation exercise, with the interrogation window sizes indicated by the 2 entries within the square brackets

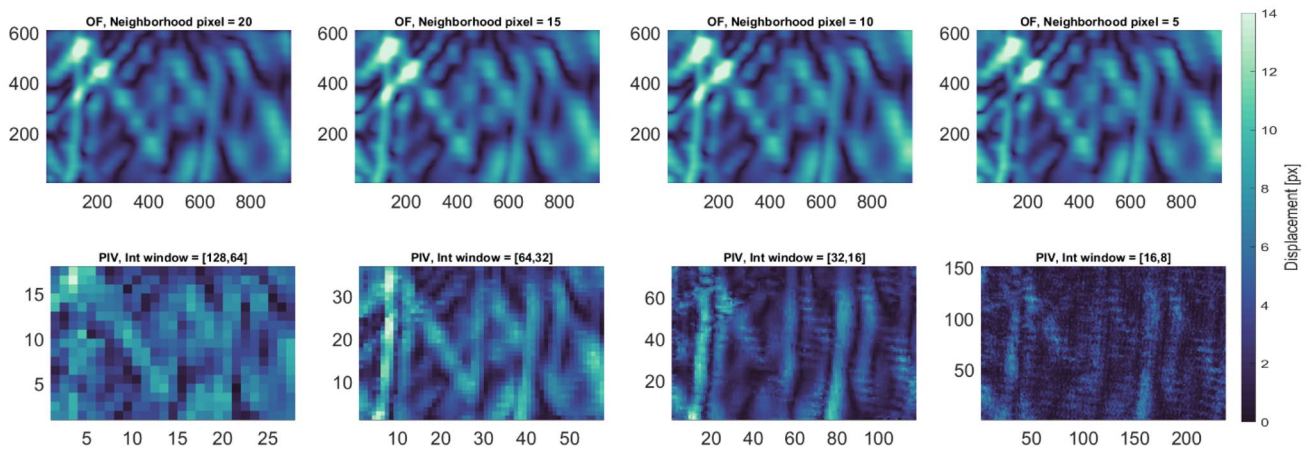
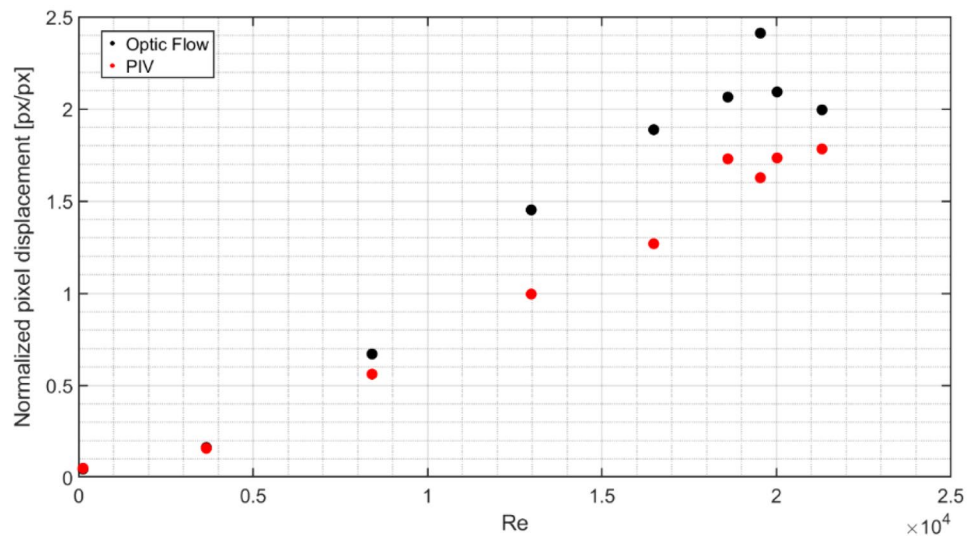


**Fig. 8** Comparison of displacement magnitude between Farneback algorithm and PIV algorithm with varying interrogation window sizes. All displacement magnitudes are shown in units of pixels. 2

passes are applied for each cross-correlation exercise, with the interrogation window sizes indicated by the 2 entries within the square brackets

**Fig. 9** Maximum displacement for increasing Reynolds number normalized by pixel size of grid element in still reference pattern



displacement vectors. Furthermore, the larger window sizes are more likely to compute reliable displacement data but at the cost of fairly low resolution. Qualitatively, it appears that the 64 and 32 interrogation window combination provide a good balance between accuracy and resolution.

In general, the Farneback algorithm captures the higher displacements more accurately as opposed to the cross-correlation algorithm. This is shown in Fig. 9 for the maximum displacements from several experimental runs with increasing  $Re$ . In this case, the parameters of the Farneback algorithm are consistent with those outlined earlier, while the cross-correlation algorithm employs 2 passes with  $64 \times 64$  pixels and  $32 \times 32$  pixels, respectively.

An important assumption regarding cross-correlation is that only uniform purely translational motion is assumed within a given interrogation window (Atcheson et al. 2009;

Scarano 2002). However, it is observed that for the submerged jet cases (Fig. 2a), significant straining and dilatation occur within the distorted checkerboard reference pattern. This is due to the generation of bump and dimple-like turbulent structures that impact the surface. The performance of the Farneback algorithm and cross-correlation is compared for a submerged jet case, as shown in Fig. 10.

From Fig. 10, regions of high strain from the distorted reference pattern image are seen to be under-predicted by the cross-correlation output, due to the failing assumption of purely translational motion. This would lead to cross-correlation algorithms being unable to accurately reconstruct a winkled free surface that is characterized by numerous bump and dimple-like structures.

Additionally, the efficiency of the Farneback algorithm compared to cross-correlation is observed to be significantly

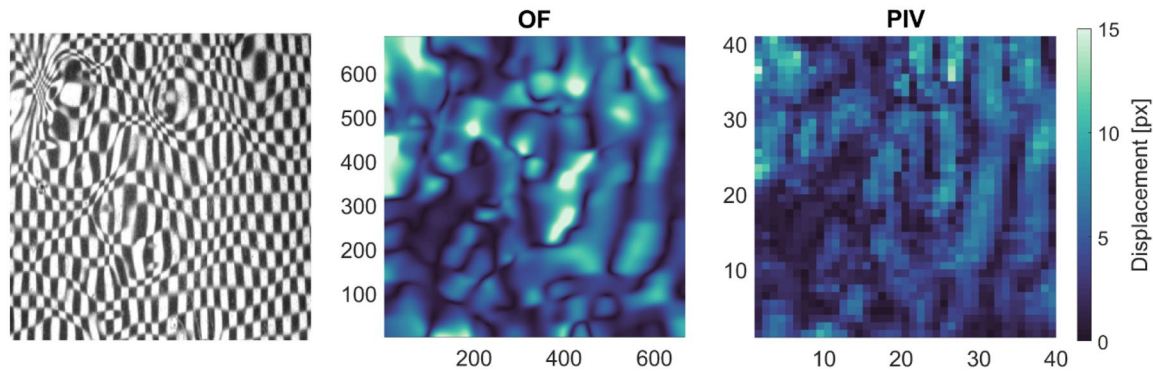


**Fig. 10** Comparison of displacement magnitude between Farneback algorithm and PIV algorithm for a submerged jet case. All displacement magnitudes are shown in pixel. 2 passes are applied for cross-correlation (64 and 32 interrogation windows)

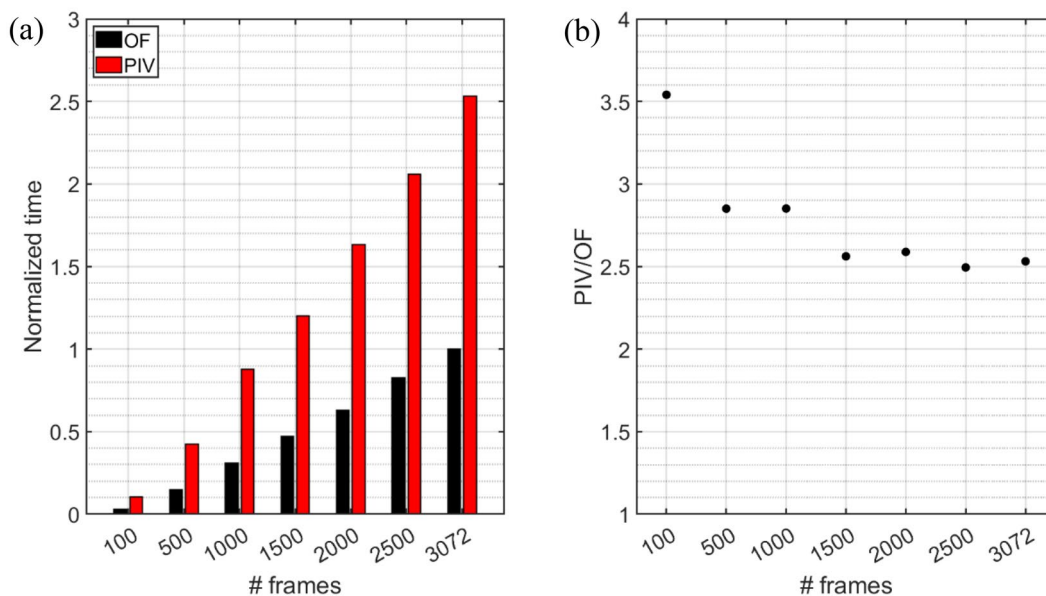


**Fig. 11** Efficiency of optic flow. **a** Computation time of varying number of frames. Results normalized by computation time of OF-3072 frames **b** ratio of computation time between PIV and OF for varying number of frames

better. This is shown in Fig. 11a for an experiment consisting of varying number of frames sampled at 50 fps. The displacement field is computed using the previously outlined Farneback parameters and a 2-pass, 64 and 32 interrogation windows with 50% overlap and parallel processing for the cross-correlation algorithm. The ratio in processing time is shown in Fig. 11b. It is seen that lower number of frames produce a higher discrepancy, and that, over higher number of frames, the ratio stabilizes around 2.5. The Farneback algorithm is therefore significantly more efficient. The computations are performed with MATLAB version 2022b running on a desktop PC with intel i7-6700 3.4 GHz processor, 32 GB RAM and an Intel HD Graphics 530 card.

In practice, and as explored in Sects. 3 and 4, high spatial resolution of  $\tilde{u}$  is advantageous in order to compute an accurate and realistic  $\eta$  domain. Additionally, for both flow conditions applied to perturb the surface (see Fig. 2), the occurrence of large displacements is expected for the ‘Fast’ flow types (see Table 1). Due to the large number of advantages proposed by the Farneback algorithm over cross-correlation (denser resolution of displacement vectors, more accurate results in terms of both high displacement and straining/dilatation areas within the domain, efficiency in processing time for large frame stacks), we make use of this algorithm to re-construct the surface profiles.



### 3 Results

#### 3.1 Free-shear flow-induced surface roughness

As discussed in Sect. 2.1, the free surface is perturbed by a free-shear flow that emanates from a submerged jet that is angled to the underside of the free surface. The output from the 3 optical setups is shown in Fig. 12 for Exp#J2, with  $Re = 6400$ . From Fig. 12, it is observed that the free surface is characterized by localized bumps and dimples (defined as sharp elevations and depressions). The free surface is rich with other surface features such as scars and ridges (line-like narrow depressions), as can be seen in the full experiment sequence presented in the supplementary material. These features are the result of the turbulent jet wrinkling the surface. The results from the two recently formulated reflection-based surface reconstruction techniques, TIR-D and M-G, are compared with the more common/established refraction-based technique, FS-SS.

There is fairly good qualitative agreement between the 3 outputs (Fig. 12a–c), as also observed in the root-squared difference of  $\eta$  (Fig. 12d, e). Across the entire experiment duration (3072 frames), there is better agreement between the TIR-D and FS-SS as opposed to the M-G and FS-SS

output. This is observed in the bin-averaged data shown in Fig. 12f, in which about 1,700,000,000 individual spatial points of  $\eta$  from 3072 temporal snapshots are sorted in descending order, and bin-averaged across every 1000 data points. We include error bars on the TIR-D and M-G results from an uncertainty analysis based on a propagation of error method that is similar to Mandel (2018).

The TIR-D output is observed to replicate the FS-SS output with more consistency across all the jet experiments, as shown in Fig. 13 (note that Fig. 12f, which is the comparisons of the 3 techniques for Exp#J2, is repeated in Fig. 13b). This is due to frames from the M-G setup possessing significant patches of image blur. The diverse turbulent features that propagate across the free surface are characterized by sharp gradients, which lead to ray-crossing in the M-G setup. The strong straining/dilatation of the surface features is more pronounced at higher  $Re$ , which explains the worsening of the M-G performance from Exp#J1 to Exp#J3. This issue has been raised in the literature regarding reflection-based techniques (Huang et al. 2023). The deviations away from the model  $y = x$  line for each of the TIR-D and M-G bin-averaged dataset from Fig. 13 are quantified in terms of the root mean square error, or RMSE. The average RMSE value across the 3 jet experiments for each of TIR-D and M-G

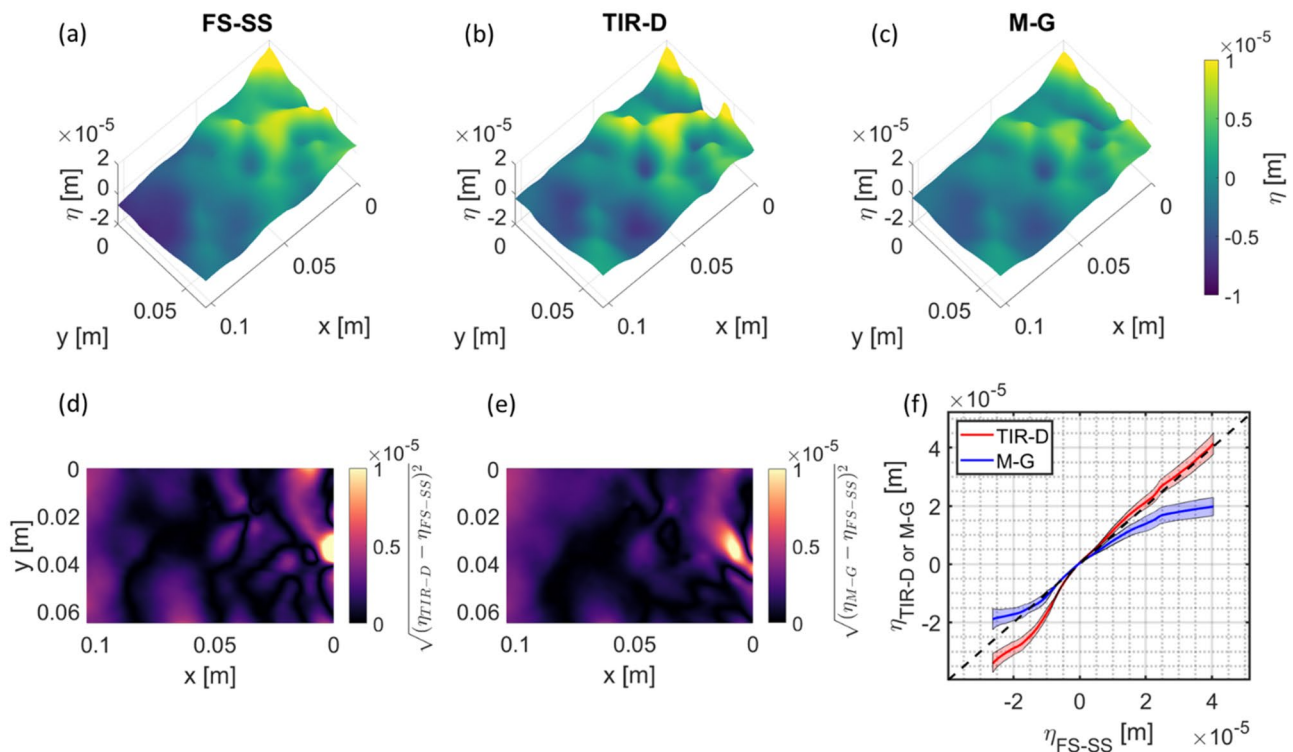
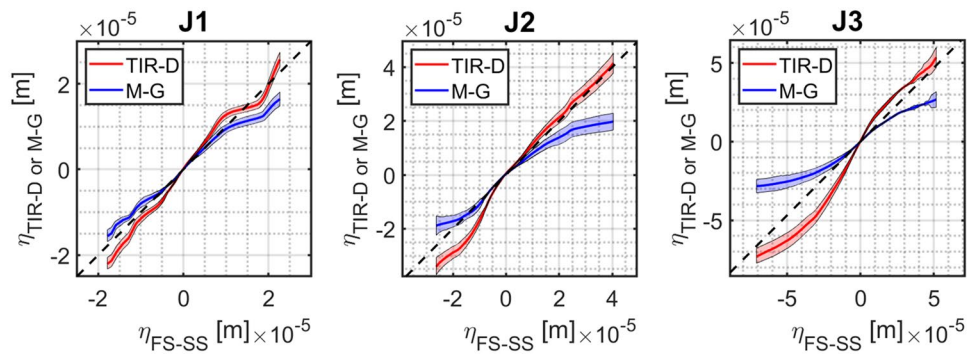


**Fig. 12** Results for Exp #J2. **a–c** snapshot of free surface from FS-SS, TIR-D and M-G, respectively; **d–e** comparison of TIR-D and M-G with FS-SS, respectively, for free surface snapshot shown in (a–c); **f** comparison of surface elevation values across entire experiment

duration between FS-SS and TIR-D/M-G. Complete set of  $\eta$  measurements across all temporal snapshots are bin averaged across 1000 elements. Solid line, bin-averaged values; shading, error bars

**Fig. 13** Comparison of bin-averaged surface elevation values across all submerged jet experiments between FS-SS and TIR-D/M-G. Solid line, bin-averaged values; shading, error bars



is  $1.8e-5$  m and  $2.0e-5$  m, respectively, with the greatest disparity between the two techniques observed for Exp#J3 (RMSE of  $2.7e-5$  m and  $3.2e-5$  m for TIR-D and M-G, respectively). This is qualitatively confirmed from Fig. 13c and can be explained by the increased patches of sharp gradients blurring the images from the M-G setup, as outlined earlier.

### 3.2 Flow overspill-induced surface waves

Here, surface waves are generated from the tube perforating the free surface. The activation of the pump induces an overspill flow, which collapses back onto the free surface and triggers radially-propagating waves. Due to the narrow transverse extent of the tank, the wavefield is characterized by wave reflections off the sidewalls, leading to an irregular wave regime, with incident waves of varying directionality. Figure 14 shows a snapshot of the free surface for Exp#W2, with  $Re = 6400$ . In this instant, the free surface consists of a wave group that is fairly unidirectional and slightly oblique to the  $y$  direction. A stark contrast in the free surface appearance is observed with respect to the jet experiment presented in Fig. 12: in this case, the free surface is purely wavy with no turbulent surface features. This can further be examined from the full experiment sequence, presented in the supplementary material.

The output from the 3 optical setups is once again observed to be fairly similar with respect to each other (Fig. 14a–c). The root-squared difference in  $\eta$  between (FS-SS–TIR-D) and (FS-SS–M-G) is seen to be fairly comparable (Fig. 14d, e) for the free surface snapshot presented in Fig. 14a–c, with higher differences observed at the upstream end of both the TIR-D and M-G domains. The complete comparison across the entire experiment duration is presented in Fig. 14f. It is seen that at lower  $\eta$  magnitudes, M-G performs better, while the TIR-D output is superior for higher magnitudes of  $\eta$ . These trends are consistent across all the wave experiments, as illustrated in Fig. 15. We note that Fig. 14f, which is the comparison of the techniques for Exp#W2, is repeated in Fig. 15b. As with the jet

experiments, the RMSE with respect to the model  $y=x$  line is performed for the bin-averaged data for TIR-D and M-G from Fig. 15. The average RMSE across all wave experiments for TIR-D and M-G are  $2.3e-5$  m and  $2.8e-5$  m, respectively. Qualitatively, it appears that, for the wave experiments, TIR-D over predicts the results, while M-G under predicts them. In general, there is a greater deviation from ground truth with increasing magnitudes of  $\eta$  for both TIR-D and M-G at high  $Re$ . This is due to larger displacements and regions of strain occurring in the images captured for both reflection-based techniques. As a result, the accuracy of the computed results tends to diminish for large surface elevation magnitudes.

### 3.3 Comparison of free surface optical techniques

The 3 optical techniques discussed so far have advantages and disadvantages over one another. For instance, due to the refraction-based approach of FS-SS, free surface features of sharper/higher surface gradients can be reconstructed, as opposed to the 2 reflection-based techniques. Sample calibrated frames taken at the same time stamp from the 3 techniques are shown in Fig. 16 for Exp#W3, the wave experiment with the highest free surface roughness. It is seen that the FS-SS frame contains the most subtle distortions, as opposed to M-G, where significant regions of image blur are observed. We speculate that this is due to the geometry of the camera with respect to the checkerboard and free surface for the case of the M-G setup. A solution to correct for the important oblique perspective of the camera field of view in the M-G configuration would be to make use of a Scheimpflug lens. This would allow for the free surface to be parallel to the image plane and consequently improve the focus over the entire free surface.

Additionally, as the camera objective is directly perpendicular to the free surface, there is no image rectification needed for the FS-SS setup, as opposed to the TIR-D and M-G field of view, where a projective transform correction needs to be applied. However, FS-SS can only be used for experiments that involve imaging a free surface that is



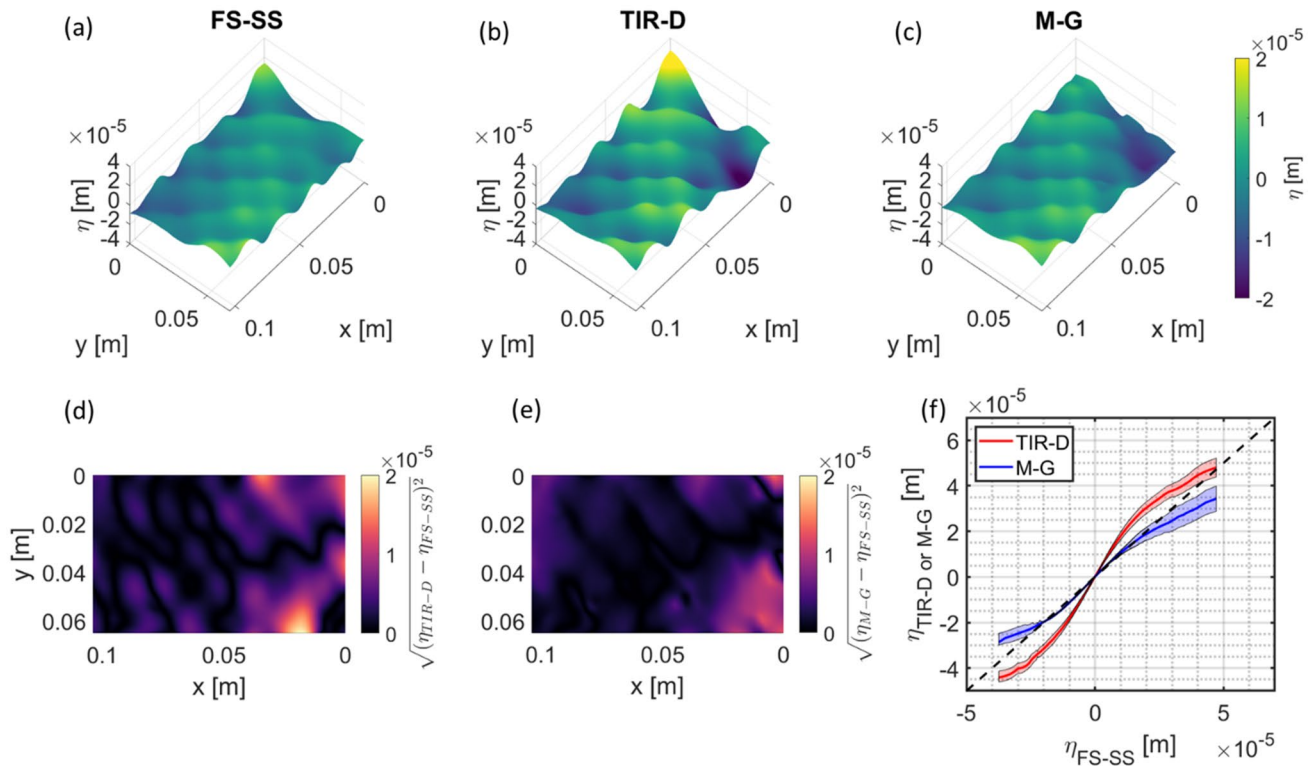


**Fig. 14** Results for Exp #W2. **a–c** snapshot of free surface from FS-SS, TIR-D and M-G, respectively; **d–e** comparison of TIR-D and M-G with FS-SS, respectively, for free surface snapshot shown in (**a–c**); **f** comparison of surface elevation values across entire experiment

directly above a clear tank bottom. In the case of an opaque tank bottom, or experiments that involve a submerged artifact, FS-SS cannot be used. Furthermore, FS-SS requires the most overhead clearance, in order to achieve the low paraxial angle approximation, as shown in (4). This often requires a more elaborate setup, which makes the camera prone to vibrations (Li et al. 2021; Moisy et al. 2009).

The TIR-D and M-G setups are both simple and straightforward. Both techniques can be used for experiments that involve a submerged object beneath the free surface. In the case of TIR-D, this assumes that the object does not occupy the entirety of the water column. As for M-G, the right illumination condition will ensure that the free surface is essentially opaque. The hypothetical scenario of a submerged canopy experiment is depicted in Fig. 24 in Appendix to portray the field of view of each setup. Additionally, the M-G technique is advantageous in the sense that the water depth needs not be known, as is the case for FS-SS and TIR-D. M-G can be used for free surface measurements over a deep liquid and can also be extended to multiphase flows of varying refractive indices. However, and as observed in Sect. 3.1, the M-G  $\eta$  output differ substantially from FS-SS for the cases of a rough free surface interface. As outlined

duration between FS-SS and TIR-D/M-G. Complete set of  $\eta$  measurements across all temporal snapshots are bin averaged across 1000 elements. Solid line, bin-averaged values; shading, error bars

previously, M-G frames are more prone to image blur over the TIR-D and FS-SS setup.

In this light, and due to future experiments that will study the free surface undulations above submerged canopy beds, we choose the TIR-D output for the deeper analysis presented in the remainder of this paper. Snapshots of the jet and wave experiments from TIR-D are presented in Figs. 17 and 18, respectively. The complete experiment sequence is presented in the supplementary material. From Fig. 17, it is observed that increasing the Re forcing leads to an increase in the severity of the surface roughness. As observed by Savelsberg and van de Water (2009), this is due to the free surface being wrinkled by the turbulent flow. Additionally, there is evidence of periodic passages of wave fronts for Exp#J3. This is explored further in Sect. 4

## 4 Discussion

The free surface behavior is inspected in the frequency domain, as shown in Fig. 19. The spectra are computed at an identical location in the middle of the domain. For the jet experiments, it is seen that Exp#J1 and J2 exhibit a near-linear slope across the frequency range, akin to an

**Fig. 15** Comparison of bin-averaged surface elevation values across all surface wave experiments between FS-SS and TIR-D/M-G. Solid line, bin-averaged values; shading, error bars

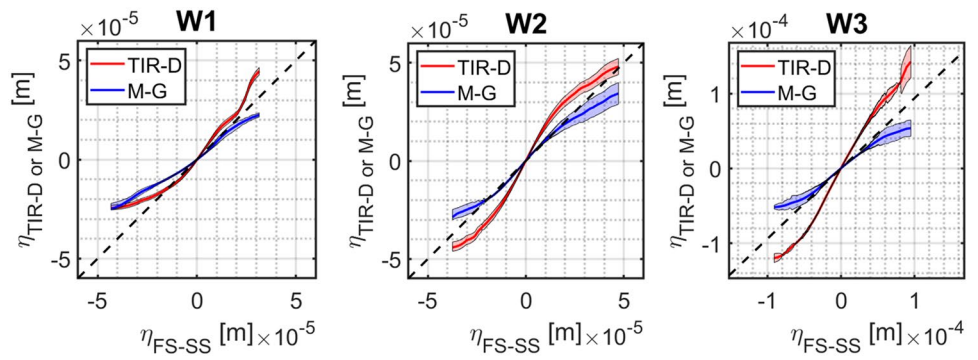


**Fig. 16** Experimental frame used for computation of displacement field taken at same time stamp for Exp#W3. **a** FS-SS; **b** TIR-D; **c** M-G

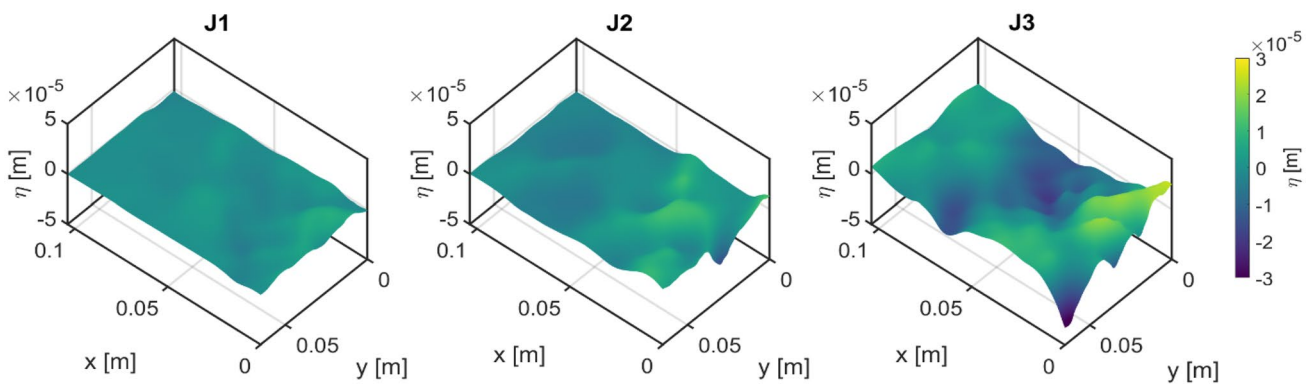
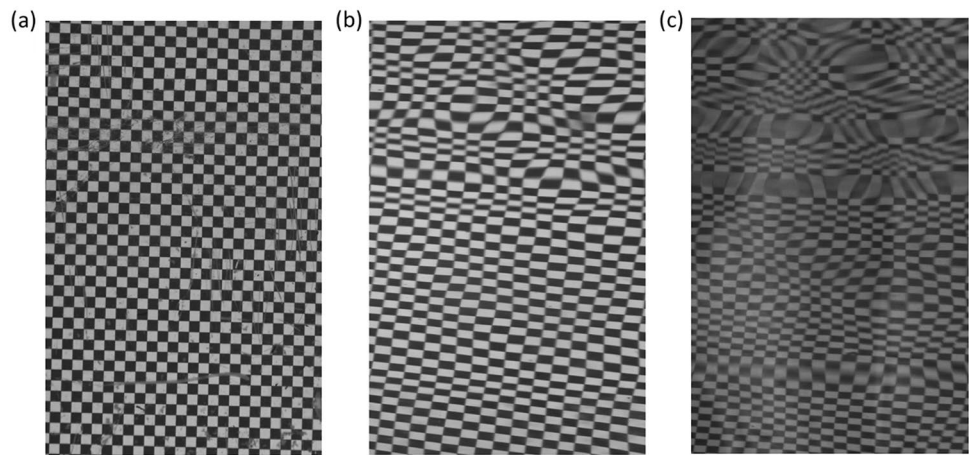


**Fig. 17** Snapshot of free surface influenced by submerged jet. Results are from TIR-D setup. An increase in surface roughness severity is noted for increasing Re

energy cascade within the inertial subrange of a turbulent flow regime. The slope of Exp#J1 and J2 are seen to be approximately  $-3$ , as shown with the reference line. This smooth decay was also reported by Dolcetti et al. (2016) from the dynamic free surface along an open channel flow. As expected, the spectral response is higher in Exp#J2, as opposed to Exp#J1, due to the more energetic free-shear flow emanating from the submerged jet. Two distinct peaks

are observed within the higher frequency band (10 Hz and 15 Hz), which we theorize are due to less prominent surface features.

The spectral signature of Exp#J3 is similar to that of Exp#J2 at the lower frequency band. However, there is a clear departure between the two spectral signatures around  $f=1.7$  Hz, where the spectrum of Exp#J3 takes on a classic wave-like behavior, as observed by the dominant frequency

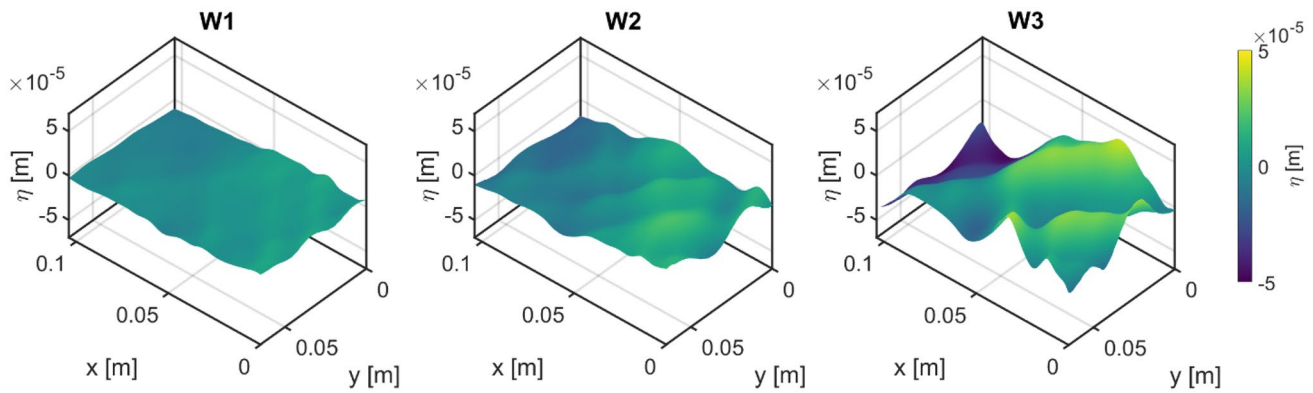
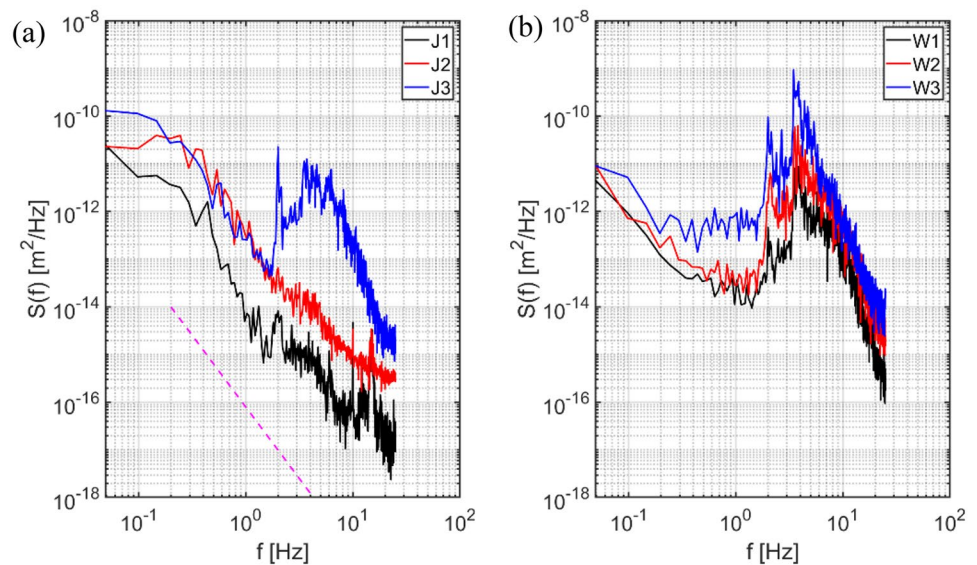


**Fig. 18** Snapshot of free surface influenced by overspill flow-induced waves. Results are from TIR-D setup. An increase in wave amplitudes is noted for increasing  $Re$

**Fig. 19** Ensemble-averaged frequency spectra. **a** jet experiments; **b** wave experiments



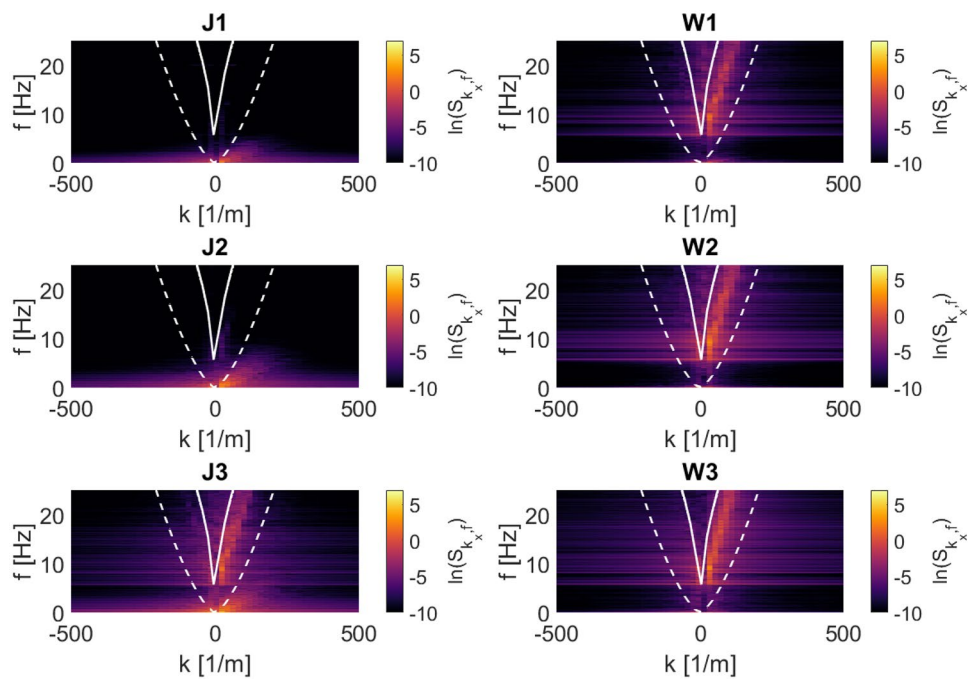
and as is seen with the comparison to the wave spectra in Fig. 19b. Exp#J3 contains a distinct peak around 2 Hz, and a broader peak with a maximum around 4 Hz. These reflect the dominant frequencies of wave-like structures that propagate across the domain and advect the turbulent surface features. This is shown in the experiment sequence in the supplementary material. The excitation mechanism of these waves has been a profound question in the recent literature. Savelsberg and van de Water (2009) proposed that the generation of random gravity-capillary waves is due to large-scale, subsurface eddies which excite these waves in all directions. This hypothesis is in line with the present experimental cases, in which the free-shear flows for Exp#J1 and J2 are not energetic enough to generate adequately large eddies. However, for Exp#J3, the free-shear flow is turbulent enough to achieve this. Another mechanism behind the generation of surface waves was proposed by Bouchet et al. (2002). As the  $Re$  of the jet is increased, an instability develops, wherein

there is an increase in the kinetic energy that is converted into potential energy. As a result, the bump located at the free surface increases in height and eventually breaks laterally, inducing periodic oscillations of the water cavity. The authors attribute this phenomenon to large deformations at the free surface along with surface waves. From Fig. 19b, it is seen that increasing the  $Re$  leads to increasing wave energetics, as is the case for the submerged jet experiments in Fig. 19a. Two localized peak frequencies are observed at  $f=2$  Hz and 4 Hz.

Streamwise transects along the tank centerline are used to compute the 2-dimensional Fourier transform. The frequency-wavenumber spectra are shown in Fig. 20 for the jet and wave experiments. As observed from the frequency spectra (Fig. 19), the spectral signature of gravity-capillary-like waves are noted in Exp#J3, while Exp#J1 and J2 only depict a linear energetic slope, which we hypothesize are that of turbulence-generated features. Recently, Dolcetti



**Fig. 20** Streamwise frequency-wavenumber spectra along centerline of domain. Solid line, gravity-capillary dispersion relation; Dash-dotted line, gravity dispersion relation; Dashed line, capillary dispersion relation



et al. (2022) proposed that the wavenumber-frequency relation of turbulence-generated water surface fluctuations can be approximated as

$$f = kU_o, \tag{11}$$

where  $U_o$  is the speed of the flow near the surface. From Fig. 20, the submerged jet speed is estimated to be of 0.025 m/s. This is computed from the slope of the turbulent signature from Exp# J1. This is an order of magnitude smaller than the wave celerity from the gravity-capillary waves, which is of about 0.25 m/s. The wave regime in Exp#J3 is observed to match those that propagate within the domain for the wave experiments. The nature of these waves is observed to not be purely gravity-capillary, as seen by the reference gravity-capillary dispersion relation. As suggested by Dolcetti et al. (2022), groups of waves with varying wavelengths and directions can combine and form complex wave patterns. The experimental domain within the tank is subjected to radially-propagating waves which undergo multiple side-wall reflections and lead to wave-wave interaction. We therefore posit that the wave regime within this study is that of complex gravity-capillary wave interactions. It is noted that at the length and temporal scales considered herein, the gravity-capillary wave dispersion relation (solid line in Fig. 20) essentially overlaps with the surface gravity wave dispersion relation (dash-dotted line in Fig. 20).

The surface waves propagate within the tank without significant mean velocity. As a result, the surface waves do not experience a Doppler shift, as would be the case for gravity-capillary waves generated along an open-channel

flow (Dolcetti et al. 2016, 2022; Dolcetti and García Nava 2019; Kidanemariam and Marusic 2020; Savelsberg and van de Water 2009). As opposed to the dual surface dynamics present in Exp#J3, the wave experiments display purely oscillatory flows, with no evidence of a turbulence signature. The combined turbulent and wave features along the free surface observed in Exp#J3 was also reported by Tani and Fujita (2018) in experiments involving river surface measurements. They observed that a major part of the free surface energy was distributed among the dispersion relation of both turbulence and gravity-capillary waves, as observed in Fig. 20 for Exp#J3.

### 5 Conclusion

The measurement of free surface elevations over a wide domain is advantageous over point measurements as it can convey information about inner-flow characteristics and bottom complexities/bathymetry and resolve small-scale wave and turbulent features. We have considered three light-based optical techniques for laboratory measurements of a free surface. FS-SS is refraction-based, while the TIR-D and M-G techniques are reflection based. To the authors' knowledge, a comparative study of optical techniques for free surface measurements has never been done. We use an optical flow algorithm, the Farneback algorithm, to make measurements of the displacement field of the free surface motions, which is then used to compute the surface elevations. Our analysis shows that the Farneback algorithm provides multiple advantages over the more classic cross-correlation

algorithm. These include density of data points, accuracy and robustness for a strongly distorted free surface, as well as computational efficiency. The two types of surface roughness considered are a rough and random free surface created by a submerged free-shear flow, along with a wavy free surface that is random/irregular.

It is seen that for a turbulent free surface characterized by bumps and dimples, the TIR-D output typically matches the FS-SS output more closely as opposed to the M-G output (average RMSE across the 3 jet experiments for TIR-D and M-G are  $1.8e-5$  m and  $2.0e-5$  m, respectively). This is because of M-G being more prone to image blur from ray crossing and diffuse reflection due to sharp/localized surface gradients. Similar to the jet experiments, TIR-D is observed to match FS-SS closer than does M-G for the wave experiments (average RMSE for TIR-D and M-G are  $2.3e-5$  m and  $2.8e-5$  m, respectively) Despite its robustness, FS-SS has certain limitations, such as requiring a significant amount of overhead clearing, the need for a clear/unobstructed tank bottom and information about the quiescent water depth. Additionally, FS-SS cannot be used for multiphase flow systems or a deep water bath. The M-G setup does not possess these limitations but is also the technique most prone to image blur, and consequently unreliable data. We therefore use the TIR-D results to analyze the free surface information in greater depth.

Notably, we observe that increasing the  $Re$  leads to an increase in the severity of the free surface roughness for the submerged jet experiments. It is seen that this is due to the subsurface turbulent flow wrinkling the free surface. The passage of periodic wavefronts is also observed for the submerged jet experiments with high  $Re$ . Possible mechanisms are outlined. First, it is seen that the generation of

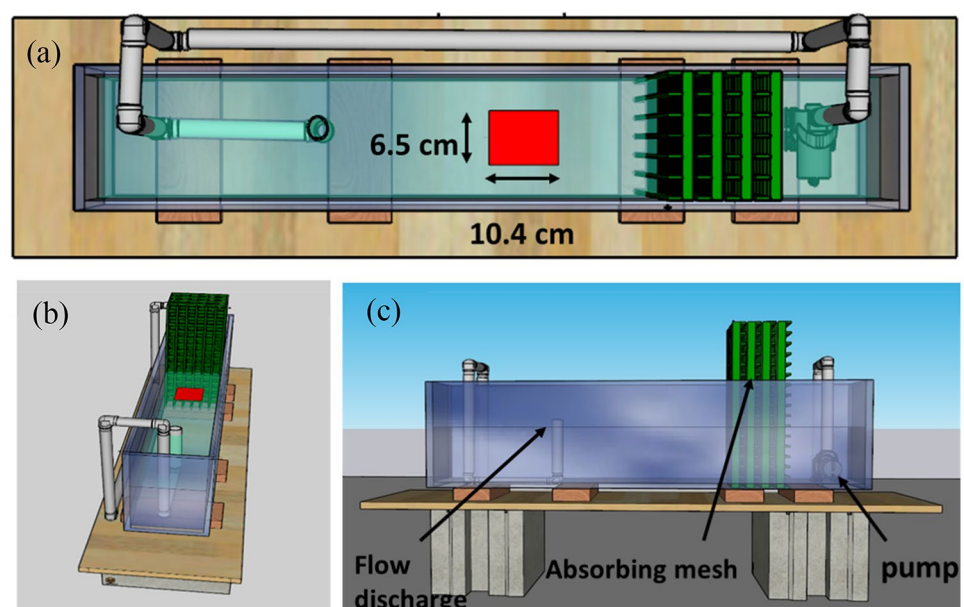
large eddies from the turbulent flow may release gravity-capillary waves in all directions. Second, it is posited that the water surface bump caused by the strong turbulent flow eventually breaks laterally and releases periodic surface motions. The spectral signature of these waves is similar to the waves generated from an emergent overspill jet. There is an order of magnitude difference in the propagation celerity of the waves over the turbulent features. We speculate that the nature of these waves is a complex interaction of gravity-capillary waves. As opposed to the submerged jet experiments with multiple surface dynamics, only oscillatory flow motion is observed from the wave experiments.

To summarize, we have assessed a suite of laboratory techniques (refraction and reflection-based) that allow for the reconstruction of dynamic and rough free surface motions. The laboratory findings obtained from such techniques can be extended to field settings. For instance, the generation and propagation of multiple surface dynamics at an air–water interface in the open ocean or coastal waters can be used to characterize the subsurface flow regime, as well as its interaction with bathymetric complexities. In the same vein, a promising area for remote measurements of the open ocean and nearshore waters will be to take advantage of the increasingly robust detection algorithms from the field of computer vision in order to achieve high spatiotemporal measurements.

## Appendix

Figures 21, 22, 23 and 24.

**Fig. 21** Experimental tank setup. **a** Plan view of tank showing domain of data capture in red, along with dimensions. **b** Perspective view of data capture domain with respect to upstream discharge. **c** Side view of tank showing flow discharge at the upstream end and pump at the downstream end. Flow is generated through tube network shown in (a). Absorbing mesh is placed close to downstream end to prevent pump-induced vibrations that may affect surface dynamics





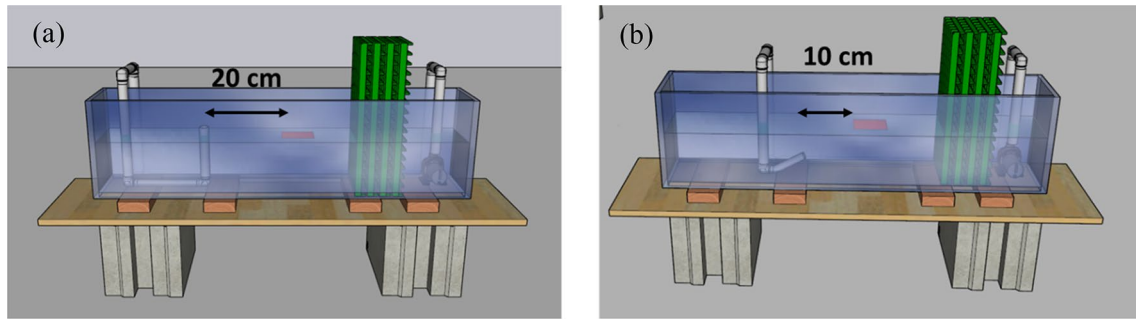


**Fig. 22** Tube network for the two surface topography generation. **a** Jet overflow-induced surface waves. Tube outlet is approximately 20 cm from upstream end of data capture domain. The tube exit is about 2 cm above the water surface. **b** Submerged jet-induced free-

shear flow. Vertical location of tube outlet is about 10 cm from upstream end of data capture domain. Tube is angled around 45° from horizontal

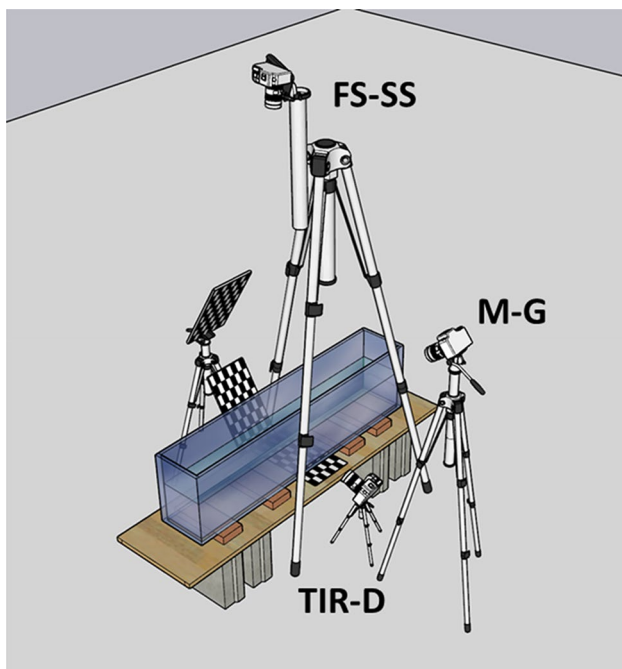


**Fig. 23** Triple optical setup for surface reconstruction. FS-SS camera is mounted onto a tripod that is placed directly above the domain of data capture. The corresponding checkerboard is placed under the tank bottom, directly under the domain of data capture. Wooden supports are placed between the tank bottom and the flat surface, to allow for the FS-SS checkerboard to be placed below the tank bottom. The M-G camera is mounted onto a tripod and is above the water-surface, angled downwards at the domain of data capture. The M-G checkerboard is mounted onto a tripod that is on the opposite side of the tank to the M-G camera. The checkerboard surface is tilted downwards at around a similar angle to that of the M-G camera. The TIR-D camera is mounted onto a smaller phone tripod and is placed below the water level, angled upwards. The TIR-D checkerboard is on the opposite side of the tank to the TIR-D camera, and is angled upwards to the free surface, at approximately the same angle as the TIR-D camera

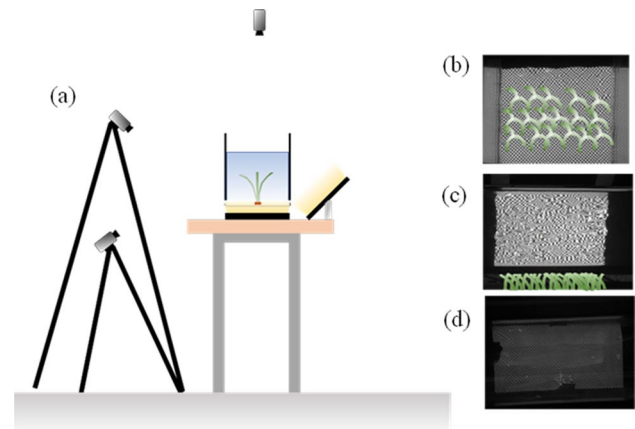


**Fig. 24** **a** Hypothetical experimental setup for free surface measurements of vegetative flows. **b–d** field of view from FS-SS, TIR-D and M-G, respectively. FS-SS contains shadow regions which makes free surface measurements unfeasible. TIR-D is spared of shadow regions, except for very tall/emergent vegetative blades. M-G can provide a fully opaque free surface for submerged vegetation cases under the right illumination conditions

**Supplementary Information** The online version contains supplementary material available at <https://doi.org/10.1007/s00348-023-03652-5>.

**Author contributions** VB contributed to study conception, design of experiments, data collection, analysis and interpretation of results, and manuscript preparation. TM contributed to study conception, design of experiments, analysis and interpretation of results, and review and editing.

**Funding** This work is supported by the Office of Naval Research under Award No. N00014-21-1-2659. We also thank N. Laxague for discussions regarding bandpass filters and frequency-wavenumber spectra computation.

**Availability of data and materials** Source code can be accessed at: <https://github.com/vab1015/Comparison-of-Optical-Techniques-for-free-surface-reconstruction.git>. Animations of the full experiments are available online in the supplementary material.

## Declarations

**Conflict of interest** The authors declare that they have no known competing financial interests or personal relationships that could have appeared to influence the work related in this paper.

**Ethical approval** Not applicable.

**Open Access** This article is licensed under a Creative Commons Attribution 4.0 International License, which permits use, sharing, adaptation, distribution and reproduction in any medium or format, as long as you give appropriate credit to the original author(s) and the source, provide a link to the Creative Commons licence, and indicate if changes were made. The images or other third party material in this article are included in the article's Creative Commons licence, unless indicated otherwise in a credit line to the material. If material is not included in the article's Creative Commons licence and your intended use is not permitted by statutory regulation or exceeds the permitted use, you will need to obtain permission directly from the copyright holder. To view a copy of this licence, visit <http://creativecommons.org/licenses/by/4.0/>.

## References

- Atcheson B, Heidrich W, Ihrke I (2009) An evaluation of optical flow algorithms for background oriented schlieren imaging. *Exp Fluids* 46(3):467–476. <https://doi.org/10.1007/s00348-008-0572-7>
- Bouchet G, Climent E, Maurel A (2002) Instability of a confined jet impinging on a water/air free surface. *Europhys Lett EPL* 59(6):827–833. <https://doi.org/10.1209/epl/i2002-00117-6>
- Brox T, Bruhn A, Papenbergh N, Weickert J (2004) High accuracy optical flow estimation based on a theory for warping. In: LNCS, vol 3024. Springer. <http://www.mia.uni-saarland.de>
- Cakir BO, Lavagnoli S, Saracoglu BH, Fureby C (2023) Assessment and application of optical flow in background-oriented schlieren for compressible flows. *Exp Fluids*. <https://doi.org/10.1007/s00348-022-03553-z>
- Chaudhari N, Ludu A, Demirkiran I (2014) A novel approach for reconstructing water surface using shape from shading technique. In: Conference proceedings—IEEE Southeastcon. <https://doi.org/10.1109/SECON.2014.6950725>
- Chetverikov D, Nagy M, Verestóy J (2000) Comparison of tracking techniques applied to digital PIV. *Proc Int Conf Pattern Recognit* 15(4):619–622. <https://doi.org/10.1109/icpr.2000.902995>
- Cobelli PJ, Maurel A, Pagneux V, Petitjeans P (2009) Global measurement of water waves by Fourier transform profilometry. *Exp Fluids* 46(6):1037–1047. <https://doi.org/10.1007/s00348-009-0611-z>
- Collignon R, Caballina O, Lemoine F, Castanet G (2022) Simultaneous temperature and thickness measurements of falling liquid films by laser-induced fluorescence. *Exp Fluids* 63(4):68. <https://doi.org/10.1007/s00348-022-03420-x>
- Cox C, Munk W (1954) Measurement of the roughness of the sea surface from photographs of the sun's glitter. *J Opt Soc Am* 44(11):838. <https://doi.org/10.1364/JOSA.44.000838>
- Dabiri D, Gharib M (2001) Simultaneous free-surface deformation and near-surface velocity measurements. In: *Experiments in fluids*, vol 30. Springer. <https://doi.org/10.1007/s003480000212>
- Dai S, Wu Y (2008) Motion from blur. *IEEE Conf Comput vis Pattern Recognit* 2008:1–8. <https://doi.org/10.1109/CVPR.2008.4587582>
- Diaz K, Chong B, Tarr S, Erickson E, Goldman DI (2022) Water surface swimming dynamics in lightweight centipedes. <https://doi.org/10.48550/arXiv.2210.09570>
- Dolcetti G, García Nava H (2019) Wavelet spectral analysis of the free surface of turbulent flows. *J Hydraul Res* 57(2):211–226. <https://doi.org/10.1080/00221686.2018.1478896>
- Dolcetti G, Horoshenkov KV, Krynkina A, Tait SJ (2016) Frequency-wavenumber spectrum of the free surface of shallow turbulent flows over a rough boundary. *Phys Fluids* 28(10):105105. <https://doi.org/10.1063/1.4964926>
- Dolcetti G, Hortobágyi B, Perks M, Tait SJ, Dervilis N (2022) Using noncontact measurement of water surface dynamics to estimate river discharge. *Water Resour Res*. <https://doi.org/10.1029/2022WR032829>
- Farnebäck G (2003) Two-frame motion estimation based on polynomial expansion. In: *Lecture notes in computer science*, pp 363–370. [https://doi.org/10.1007/3-540-45103-X\\_50](https://doi.org/10.1007/3-540-45103-X_50)
- Gomit G, Chatellier L, Calluau D, David L (2013) Free surface measurement by stereo-refraction. *Exp Fluids*. <https://doi.org/10.1007/s00348-013-1540-4>
- Gomit G, Chatellier L, David L (2022) Free-surface flow measurements by non-intrusive methods: a survey. *Exp Fluids* 63(6):94. <https://doi.org/10.1007/s00348-022-03450-5>
- Horn BKP, Schunck BG (1981) Determining optical flow. *Artif Intell* 17(1–3):185–203. [https://doi.org/10.1016/0004-3702\(81\)90024-2](https://doi.org/10.1016/0004-3702(81)90024-2)
- Huang Y, Huang X, Zhong M, Liu Z (2023) A bilayer color digital image correlation method for the measurement of the topography of a liquid interface. *Opt Lasers Eng* 160:107242. <https://doi.org/10.1016/j.optlaseng.2022.107242>
- Jain U (2020) Slamming liquid impact and the mediating role of air. Doctoral dissertation, Universiteit Twente. <https://doi.org/10.3990/1.9789036550215>
- Jain U, Gauthier A, Lohse D, van der Meer D (2021a) Air-cushioning effect and Kelvin–Helmholtz instability before the slamming of a disk on water. *Phys Rev Fluids*. <https://doi.org/10.1103/PhysRevFluids.6.L042001>
- Jain U, Gauthier A, van der Meer D (2021b) Total-internal-reflection deflectometry for measuring small deflections of a fluid surface. *Exp Fluids* 62(11):1–14. <https://doi.org/10.1007/s00348-021-03328-y>
- Jain U, Vega-Martínez P, van der Meer D (2021c) Air entrapment and its effect on pressure impulses in the slamming of a flat disc on water. *J Fluid Mech* 928:31. <https://doi.org/10.1017/jfm.2021.846>
- Jain U, Novaković V, Bogaert H, van der Meer D (2022) On wedgeslamming pressures. *J Fluid Mech* 934:A27. <https://doi.org/10.1017/jfm.2021.1129>
- Kidanemariam A, Marusic I (2020) On the turbulence-generated free-surface waves in open-channel flows. In: *Proceedings of the 22nd Australasian fluid mechanics conference AFMC2020*. <https://doi.org/10.14264/0912f75>
- Kochkin D, Mungalov A, Zaitsev D, Kabov O (2022) Use of the reflective background oriented schlieren technique to measure free surface deformations in a thin liquid layer non-uniformly heated from below. *Exp Therm Fluid Sci* 133:110576. <https://doi.org/10.1016/j.expthermflusci.2021.110576>
- Kurata J, Grattan KTV, Uchiyama H, Tanaka T (1990) Water surface measurement in a shallow channel using the transmitted image of a grating. *Rev Sci Instrum* 61(2):736–739. <https://doi.org/10.1063/1.1141487>
- Laxague NJM, Zappa CJ, LeBel DA, Banner ML (2018) Spectral characteristics of gravity-capillary waves, with connections to wave growth and microbreaking. *J Geophys Res Oceans* 123(7):4576–4592. <https://doi.org/10.1029/2018JC013859>

- Li H, Avila M, Xu D (2021) A single-camera synthetic Schlieren method for the measurement of free liquid surfaces. *Exp Fluids* 62(11):227. <https://doi.org/10.1007/s00348-021-03326-0>
- Liu T, Merat A, Makhmalbaf MHM, Fajardo C, Merati P (2015) Comparison between optical flow and cross-correlation methods for extraction of velocity fields from particle images. *Exp Fluids* 56(8):1–23. <https://doi.org/10.1007/s00348-015-2036-1>
- Lucas BD, Kanade T (1981) An iterative image registration technique with an application to stereo vision. In: Proceedings of the 7th international joint conference on artificial intelligence, pp 674–679. <https://doi.org/10.5555/1623264.1623280>
- Mandel TL (2018) Free surface dynamics in the presence of submerged canopies. Doctoral dissertation, Stanford University, Stanford, CA. <http://purl.stanford.edu/nj520rc8168>
- Mandel TL, Rosenzweig I, Chung H, Ouellette NT, Koseff JR (2017) Characterizing free-surface expressions of flow instabilities by tracking submerged features. *Exp Fluids* 58(11):1–14. <https://doi.org/10.1007/s00348-017-2435-6>
- Mandel TL, Gakhar S, Chung H, Rosenzweig I, Koseff JR (2019) On the surface expression of a canopy-generated shear instability. *J Fluid Mech* 867:633–660. <https://doi.org/10.1017/jfm.2019.170>
- McIlvenny J, Williamson BJ, Fairley IA, Lewis M, Neill S, Masters I, Reeve DE (2022) Comparison of dense optical flow and PIV techniques for mapping surface current flow in tidal stream energy sites. *Int J Energy Environ Eng*. <https://doi.org/10.1007/s40095-022-00519-z>
- Mendez MA, Scheid B, Buchlin JM (2017) Low Kapitzza falling liquid films. *Chem Eng Sci* 170:122–138. <https://doi.org/10.1016/j.ces.2016.12.050>
- Metzmacher J, Lagubeau G, Poty M, Vandewalle N (2022) Double pattern improves the Schlieren methods for measuring liquid–air interface topography. *Exp Fluids* 63(8):120. <https://doi.org/10.1007/s00348-022-03467-w>
- Moisy F, Rabaud M, Salsac K (2009) A synthetic Schlieren method for the measurement of the topography of a liquid interface. *Exp Fluids* 46(6):1021–1036. <https://doi.org/10.1007/s00348-008-0608-z>
- Mouza AA, Vlachos NA, Paras SV, Karabelas AJ (2000) Measurement of liquid film thickness using a laser light absorption method. *Exp Fluids* 28(4):355–359. <https://doi.org/10.1007/s003480050394>
- Mungalov AS, Derevyannikov IA (2021) Reflective synthetic schlieren technique for measuring liquid surface deformations. *AIP Erence Proc* 2422:040012. <https://doi.org/10.1063/5.0068194>
- Muraro F, Dolcetti G, Nichols A, Tait SJ, Horoshenkov KV (2021) Free-surface behaviour of shallow turbulent flows. *J Hydraul Res* 59(1):1–20. <https://doi.org/10.1080/00221686.2020.1870007>
- Nie X, Hu Y, Su Z, Shen X (2021) Fluid reconstruction and editing from a monocular video based on the SPH model with external force guidance. *Comput Graph Forum* 40(6):62–76. <https://doi.org/10.1111/cgf.14203>
- Paquier A, Moisy F, Rabaud M (2015) Surface deformations and wave generation by wind blowing over a viscous liquid. *Phys Fluids* 27(12):122103. <https://doi.org/10.1063/1.4936395>
- Pathommapas C, Yapo S, Seesomboon E, Pussadee N (2019) Application of free surface synthetic schlieren method in determining surface tension from a light floating object. *J Phys Conf Ser* 1380(1):012109. <https://doi.org/10.1088/1742-6596/1380/1/012109>
- Pickup D, Li C, Cosker D, Hall P, Willis P (2011) Reconstructing mass-conserved water surfaces using shape from shading and optical flow. In: Lecture notes in computer science, pp 189–201. [https://doi.org/10.1007/978-3-642-19282-1\\_16](https://doi.org/10.1007/978-3-642-19282-1_16)
- Rosegen T, Lang A, Gharib M (1998) Fluid surface imaging using microlens arrays. *Exp Fluids* 25:126–132. <https://doi.org/10.1007/s003480050216>
- Rudenko YK, Vinnichenko NA, Plaksina YY, Pushtaev AV, Uvarov AV (2022) Horizontal convective flow from a line heat source located at the liquid–gas interface in presence of surface film. *J Fluid Mech* 944:407–422. <https://doi.org/10.1017/jfm.2022.502>
- Ruhnau P, Kohlberger T, Schnörr C, Nobach H (2005) Variational optical flow estimation for particle image velocimetry. *Exp Fluids* 38(1):21–32. <https://doi.org/10.1007/s00348-004-0880-5>
- Rupnik E, Jansa J, Pfeifer N (2015) Sinusoidal wave estimation using photogrammetry and short video sequences. *Sensors (switzerland)* 15(12):30784–30809. <https://doi.org/10.3390/s151229828>
- Savelsberg R, van de Water W (2009) Experiments on free-surface turbulence. *J Fluid Mech* 619:95–125. <https://doi.org/10.1017/S0022112008004369>
- Scarano F (2002) Iterative image deformation methods in PIV. *Meas Sci Technol* 13(1):R1–R19. <https://doi.org/10.1088/0957-0233/13/1/201>
- Shimazaki T, Ichihara S, Tagawa Y (2022) Background oriented schlieren technique with fast Fourier demodulation for measuring large density-gradient fields of fluids. *Exp Therm Fluid Sci* 134:110598. <https://doi.org/10.1016/j.exptthermflusci.2022.110598>
- Tani K, Fujita I (2018) Wavenumber-frequency analysis of river surface texture to improve accuracy of image-based velocimetry. *E3S Web Conf* 40:06012. <https://doi.org/10.1051/e3sconf/20184006012>
- The MathWorks Inc (2022) MATLAB version: 9.13.0 (R2022b), Natick, Massachusetts: The MathWorks Inc. <https://www.mathworks.com>
- Thielicke W, Sonntag R (2021) Particle image velocimetry for MATLAB: accuracy and enhanced algorithms in PIVlab. *J Open Res Softw* 9:1–14. <https://doi.org/10.5334/JORS.334>
- Turney DE, Anderer A, Banerjee S (2009) A method for three-dimensional interfacial particle image velocimetry (3D-PIV) of an air–water interface. *Meas Sci Technol* 20(4):045403. <https://doi.org/10.1088/0957-0233/20/4/045403>
- Vinnichenko NA, Pushtaev AV, Plaksina YY, Uvarov AV (2020) Measurements of liquid surface relief with moon-glade background oriented Schlieren technique. *Exp Therm Fluid Sci* 114:110051. <https://doi.org/10.1016/j.exptthermflusci.2020.110051>
- Wildeman S (2018) Real-time quantitative Schlieren imaging by fast Fourier demodulation of a checked backdrop. *Exp Fluids* 59(6):97. <https://doi.org/10.1007/s00348-018-2553-9>
- Wu H, Zhao R, Gan X, Ma X (2019) Measuring surface velocity of water flow by dense optical flow method. *Water (switzerland)* 11(11):2320. <https://doi.org/10.3390/w11112320>
- Xue T, Li Z, Li C, Wu B (2019) Measurement of thickness of annular liquid films based on distortion correction of laser-induced fluorescence imaging. *Rev Sci Instrum* 90(3):033103. <https://doi.org/10.1063/1.5063383>
- Zhang X (1996) An algorithm for calculating water surface elevations from surface gradient. In: Experiments in Fluids, Vol. 21. Springer-Verlag. <https://doi.org/10.1007/BF00204634>
- Zhang X, Cox CS (1994) Measuring the two-dimensional structure of a wavy surface optically: A surface gradient detector. *Exp Fluids* 7:225–237. <https://doi.org/10.1007/BF00203041>
- Zhang X, Dabiri D, Gharib M (1996) Optical mapping of fluid density interfaces: concepts and implementations. *Rev Sci Instrum* 67(5):1858–1868. <https://doi.org/10.1063/1.1146990>
- Zhang Z, Chang C, Liu X, Li Z, Shi Y, Gao N, Meng Z (2021) Phase measuring deflectometry for obtaining 3D shape of specular surface: a review of the state-of-the-art. *Opt Eng* 60(02):020903. <https://doi.org/10.1117/1.oe.60.2.020903>